

# X-ray spectral properties of the AGN sample in the northern XMM-XXL field

Zhu Liu,<sup>1,2,3\*</sup> Andrea Merloni,<sup>3,†</sup> Antonis Georgakakis,<sup>3,4</sup> Marie-Luise Menzel,<sup>3</sup>  
 Johannes Buchner,<sup>3</sup> Kirpal Nandra,<sup>3</sup> Mara Salvato,<sup>3</sup> Yue Shen,<sup>5,6,‡</sup> Marcella Brusa,<sup>3,7,8</sup>  
 Alina Streblyanska<sup>9,10</sup>

<sup>1</sup>National Astronomical Observatories, Chinese Academy of Sciences, Beijing 100012, People's Republic of China

<sup>2</sup>University of Chinese Academy of Sciences, Beijing 100049, People's Republic of China

<sup>3</sup>Max-Planck-Institut für extraterrestrische Physik, Giessenbachstrasse 1, D-85748, Garching bei München, Germany

<sup>4</sup>IAASARS, National Observatory of Athens, GR-15236 Penteli, Greece

<sup>5</sup>Carnegie Observatories, 813 Santa Barbara Street, Pasadena, CA 91101, USA

<sup>6</sup>Kavli Institute for Astronomy and Astrophysics, Peking University, Beijing 100871, People's Republic of China

<sup>7</sup>Dipartimento di Fisica e Astronomia, Università di Bologna, viale Berti Pichat 6/2, I-40127 Bologna, Italy

<sup>8</sup>INAF Osservatorio Astronomico di Bologna, via Ranzani 1, I-40127 Bologna, Italy

<sup>9</sup>Instituto de Astrofísica de Canarias (IAC), E-38200 La Laguna, Tenerife, Spain

<sup>10</sup>Departamento de Astrofísica, Universidad de La Laguna (ULL), E-38205 La Laguna, Tenerife, Spain

Accepted XXX. Received YYY; in original form ZZZ

## ABSTRACT

In this paper we describe and publicly release a catalogue consisting of 8445 point-like X-ray sources detected in the XMM-XXL north survey. For the 2512 AGN which have reliable spectroscopy from SDSS-III/BOSS, we present the X-ray spectral fitting which has been computed with a Bayesian approach. We have also applied an X-ray spectral stacking method to different sub-samples, selected on the basis of the AGN physical properties ( $L_{2-10\text{keV}}$ ,  $z$ ,  $M_{\text{BH}}$ ,  $\lambda_{\text{Edd}}$  and  $N_{\text{H}}$ ). We confirm the well-known Iwasawa-Taniguchi effect in our luminosity-redshift sub-samples, and argue that such an effect is due to a decrease in the covering factor of a distant obscuring ‘torus’ with increasing X-ray luminosity. By comparing the distribution of the reflection fraction, the ratio of the normalization of the reflected component to the direct radiation, we find that the low-luminosity, low-redshift sub-sample had systematically higher reflection fraction values than the high-redshift, high-luminosity one. On the other hand, no significant difference is found between samples having similar luminosity but different redshift, suggesting that the structure of the torus does not evolve strongly with redshift. Contrary to previous works, we do not find evidence for an increasing photon index at high Eddington ratio. This may be an indication that the structure of the accretion disc changes as the Eddington ratio approaches unity. Comparing our X-ray spectral analysis results with the optical spectral classification, we find that  $\sim 20$  per cent of optical type-1 AGN show an X-ray absorbing column density higher than  $10^{21.5}\text{ cm}^{-2}$ , and about 50 per cent of type-2 AGN have an X-ray absorbing column density less than  $10^{21.5}\text{ cm}^{-2}$ . We suggest that the excess X-ray absorption shown in the high-luminosity optical type-1 AGN can be due to small-scale dust-free gas within (or close to) the broad line region, while in the low-luminosity ones it can be due to a clumpy torus with a large covering factor.

**Key words:** galaxies: active – X-rays: galaxies

## 1 INTRODUCTION

Active galactic nuclei (AGN) are among the most luminous objects in the Universe and emit radiation over the whole range of the electromagnetic spectrum. They are believed to be powered by accretion of matter on to a super-massive black hole (SMBH). It

\* liuzhu@nao.cas.cn(ZL)

† am@mpe.mpg.de(AM)

‡ Hubble Fellow

is now well established that almost all massive galaxies harbour a SMBH at their centre (Kormendy & Richstone 1995). This leads to the suggestion that most galaxies have been through a phase of nuclear activity in the past (Marconi et al. 2004; Merloni & Heinz 2008; Shankar 2009), and that SMBH growth is mainly due to accretion of matter during active phases over cosmological times.

AGN are powerful X-ray emitters which dominate the source number counts in the distant X-ray source populations. Because X-ray emission is less diluted by the host-galaxy starlight and absorption of the material along the line of sight, X-ray surveys of AGN provide the most complete and unbiased AGN census (Brandt & Alexander 2015). Thanks to the improved sensitivity and resolution of X-ray missions such as *X-ray Multi-Mirror Mission (XMM-Newton)*; e.g. Jansen et al. 2001) and *Chandra X-ray Observatory* (Chandra; e.g. Weisskopf et al. 2000), X-ray surveys are now able to detect large numbers of AGN over a wide range of redshifts, providing a powerful tool for studying the evolution of SMBH and their host galaxies.

Observationally, the main feature in the X-ray spectra of AGN is a power-law continuum, which is presented as  $N(E) \propto E^{-\Gamma}$ . This power-law component is thought to be produced by inverse Comptonization of optical/UV photons in a hot corona located close to the accretion disc (e.g. Haardt & Maraschi 1991). Investigations of the relation between the power-law photon index,  $\Gamma$ , and the other AGN physical parameters, e.g. the Eddington ratio  $\lambda_{\text{Edd}}$ <sup>1</sup> and X-ray luminosity  $L_X$ , may yield important insights into the accretion processes and the corona properties. Previous works have shown that  $\Gamma$  is anti-correlated with  $\lambda_{\text{Edd}}$  when  $\lambda_{\text{Edd}} \lesssim 10^{-3} - 10^{-2}$  (Gu & Cao 2009) and strongly correlated with  $\lambda_{\text{Edd}}$  when  $\lambda_{\text{Edd}} > 10^{-3} - 10^{-2}$  (Lu & Yu 1999; Shemmer et al. 2006, 2008; Wu & Gu 2008; Risaliti, Young, & Elvis 2009; Zhou & Zhao 2010; Brightman et al. 2013; Jin, Ward, & Done 2012; Fanali et al. 2013). However, Ai et al. (2011) suggested that the relation may be flatter if  $\lambda_{\text{Edd}}$  is higher than  $\sim 1.0$ . This suggestion was strengthened by Kamizasa, Terashima, & Awaki (2012) using a sample of sources with low BH masses and high  $\lambda_{\text{Edd}}$ . The relation between  $\Gamma$  and  $\lambda_{\text{Edd}}$  in the high  $\lambda_{\text{Edd}}$  regime is therefore still unclear, but could hold important clues on the physical properties of near-Eddington accretors.

In addition to the power-law continuum, other spectral features, such as absorption, reflection and soft X-ray excess are also present in the X-ray spectra of AGN. A significant fraction of X-ray radiation will be absorbed or scattered by the material along the line of sight between the X-ray source and the observer (e.g. Turner et al. 1997; Risaliti, Maiolino, & Salvati 1999; Turner & Miller 2009). The primary effect of absorption on the X-ray spectrum is the cut-off of the emission at low energies if absorbed by neutral material, or resonant absorption lines and edges from ionized elements if the material is ionized/warm gas, making it possible to measure the amount of material along line of sight through X-ray data. The reflection component is produced through Compton scattering of X-ray photons into the line of sight by optically thick material. It will be most significant in the 5-50 keV range with a peak at around 30 keV (Krolik 1999, the so-called Compton hump). The 6.4 keV fluorescent Fe  $K\alpha$  line, which is expected if reflection is important (George, Fabian, & Nandra 1990), is the most prominent emission line in the X-ray spectra of AGN (Pounds et al. 1990; Nandra & Pounds 1994). Many previous studies found that the equivalent width (EW) of the narrow Fe  $K\alpha$  line, which is

believed to be produced in the inner wall of the torus, i.e. an optical thick dusty cloud surrounding the nucleus on parsec-scale, is anti-correlated with the 2 – 10 keV X-ray luminosity (the X-ray Baldwin effect or Iwasawa-Taniguchi effect, e.g. Iwasawa & Taniguchi 1993; Page et al. 2004; Bianchi et al. 2007; Shu, Yaqoob, & Wang 2010, 2011; Falocco et al. 2013). The origin of this correlation is still unclear, with one possible explanation being the decrease of the covering factor of the torus with the X-ray luminosity (Page et al. 2004; Zhou & Wang 2005; Ricci et al. 2013a). A broad Fe  $K\alpha$  line is also found in roughly  $\sim 45$  per cent of AGN (Nandra et al. 2007; de La Calle Pérez et al. 2010; Patrick et al. 2012), whose archetypes include MCG-6-30-15 (Tanaka et al. 1995), 1H 0707-495 (Fabian et al. 2009) and others (e.g. Nandra et al. 2007; Patrick et al. 2012). Unlike the narrow Fe  $K\alpha$  line, the broad Fe  $K\alpha$  line is generally thought to originate from the inner region of the accretion disc (Fabian et al. 1989), and to be broadened by the motion induced by the strong gravitational field of the central SMBH (alternative explanations have also been proposed, however; e.g. Miller et al. 2008 showed that the emergence of a broad profile can be due to complex absorption. The broad line profile can also be well fitted with a Compton-thick wind model, see Tatum et al. 2012). The line profile of the broad Fe  $K\alpha$  line can be used to constrain the spin of the black hole (BH; e.g. Brenneman & Reynolds 2006; Dauser et al. 2010). All these observed X-ray spectral features, which are likely to originate from the central region of AGN, offer the best chance to study the immediate environment of SMBH and the poorly understood accretion process.

AGN are traditionally divided into different types on the basis of the observed properties, e.g. type-1 and type-2 based on the optical emission line, radio-loud and radio-quiet depending on the radio radiation. The unification model of AGN explains the different types by the orientation of the observer with respect to the torus (Antonucci 1993; Urry & Padovani 1995). In this scheme all the different types of AGN have the same central engine (SMBH) and small scale broad-line region (BLR). The type-1 AGN is seen from inclination angles which are not obscured by the torus, showing signature of broad-emission lines in the optical spectra. Conversely, the broad lines are hidden in type-2 AGN, for which the obscuration by the torus is in the line of sight, and only the high-excitation lines produced in the narrow-line region on much larger scales can be observed. The detection of polarized broad-emission lines in the optical spectra of type-2 AGN, showing the existence of BLR, is the key piece of evidence for the unification scenario (Antonucci & Miller 1985). It is also supported by the observed X-ray spectra, which show substantial obscuration in type-2 galaxies. However, results based on larger and deeper X-ray surveys show evidences that the fraction of absorbed AGN appeared to decrease with X-ray luminosity (Ueda et al. 2003; Akylas et al. 2006; Hasinger 2008; Bongiorno et al. 2010; Brusa et al. 2010; Merloni et al. 2014; Buchner et al. 2015) which seems to be at odds with the simple unification model. Using an AGN sample selected from the XMM-COSMOS survey, Merloni et al. (2014) found that a large fraction ( $\sim 30$  per cent) of the sources show discrepancies between the optical and X-ray classifications. These results suggest that the simple unification-by-orientation scheme is not enough to explain all the observed phenomena, and other physical parameters may play an important role.

In this work, we describe a catalogue including 8445 point-like X-ray sources detected in the XMM-XXL survey in the Northern hemisphere (hereinafter: XXL-N). We also present a study of the X-ray properties of a large AGN sample selected from the XXL-N so as to understand the X-ray Baldwin effect, the impact of ac-

<sup>1</sup>  $\lambda_{\text{Edd}} = L_{\text{bol}}/L_{\text{Edd}}$ , where  $L_{\text{Edd}} = 1.3 \times 10^{38} (M_{\text{BH}}/M_{\odot})$  and  $L_{\text{bol}}$  is the bolometric luminosity.

cretion rate on the structure of accretion disc and the discrepancy between the optical and X-ray classification of AGN. The XXL-N survey, along with the dedicated Sloan Digital Sky Survey (SDSS) ancillary follow-up programme (Menzel et al. 2016), provide one of the largest X-ray detected AGN samples with reliable optical redshift measurements and classifications, making it possible to investigate the X-ray properties of AGN spanning a wide region of parameter space. The large area covered by the survey, compared to most well-studied X-ray deep fields, also provides a unique sample of the rare AGN population, sampling the most luminous, highest  $\lambda_{\text{Edd}}$  objects.

This paper is structured as follows, In Section 2, we introduce the XXL-N survey. Furthermore, we describe the X-ray data reduction as well as source detection. The optical cross-matching, data reduction and  $M_{\text{BH}}$  estimation are presented in Section 3. The full list of the point-like X-ray sources catalogue is also included in this section. The X-ray spectral analysis for each individual source with reliable redshift measurement is described in Section 4, while in Section 5, we present the results from X-ray spectral stacking for the type-1 AGN sample. We present the discussion and summary of our results in Sections 6 and 7, respectively. Throughout this paper, we use the cosmological parameters  $H_0 = 70 \text{ km s}^{-1} \text{ Mpc}^{-1}$ ,  $\Omega_{\text{M}} = 0.27$  and  $\Omega_{\Lambda} = 0.73$ . All quoted errors correspond to the 68 per cent confidence level unless specified otherwise.

## 2 SOURCE DETECTION AND DATA REDUCTION

### 2.1 Source detection

The X-ray selected AGN sample used in this paper is compiled from the wide-area and shallow XXL-N survey (Pierre et al. 2015). This programme covers a total of about  $50 \text{ deg}^2$  with an exposure time of about 10 ks per XMM pointing. The surveyed area is split into two fields nearly equal in size. In this paper we present the source catalogue of the equatorial subregion of the XXL-N, which overlaps with the Canada-France-Hawaii Legacy Survey (CFHTLS) W1 field and extends to about  $25 \text{ deg}^2$  the area covered by the original  $11 \text{ deg}^2$  XMM-LSS survey (Clerc et al. 2014). The X-ray survey layout is presented in Fig. 1.

The data reduction, source detection, identification of the X-ray sources with optical counterparts and sensitivity map construction follow the methods described in Georgakakis & Nandra (2011). The most salient details of those steps are outlined in this section. The XMM observations are reduced using the XMM-Newton Science Analysis System (SAS) version 12 (Gabriel et al. 2004). XXL-N data observed prior to 23 January 2012 are analysed. At that date the XXL-N programme was partially complete. As a result the final catalogue of the XXL-N field presented in this paper is missing about  $5 \text{ deg}^2$  worth of X-ray data. This incomplete data coverage is shown by the dark stripes in Fig. 1. Appendix A lists the individual XMM observations used in this paper. Our reduction is not limited to the XXL-N/XMM-LSS 10 ks data only but includes deeper XMM observations within the XXL-N footprint, such as the Subaru/XMM-Newton Deep Survey Field (SXDS, Ueda et al. 2008). Additionally any overlapping XMM observations are merged using the SAS task EMOSAIC as explained in Georgakakis & Nandra (2011) to increase the point source sensitivity of the final catalogue. The first step of the data reduction process is the production of event files from the Observation Data Files (ODF) using the EPCHAIN and EMCHAIN tasks of SAS for the EPIC (European Photon Imaging Camera, Strüder et al. 2001; Turner

et al. 2001) PN and MOS detectors respectively. Pixels along the edges of the CCDs of the PN and MOS detectors are removed because their inclusion often results to spurious detections. Flaring background periods are identified using a methodology similar to that described in Nandra et al. (2007). First, the EWAVLET task of SAS with a threshold of 5 times the local background rms is used to detect sources in the  $0.5 - 8 \text{ keV}$  spectral band of the combined image of all EPIC detectors available to a particular XMM observation. These sources are then masked out from the event file before generating the background light curve. The approximate quiescent background level is determined by calculating the count rate at which the excess variance of the background light curve is minimum. Periods with background count rate 2 times higher than the level where the excess variance is minimum are excluded from the filtered event file (see Georgakakis & Nandra 2011, for more details). Images and exposure maps in celestial coordinates with pixel size of 4.35 arcsec are constructed in 5 energy bands,  $0.5 - 8$  (full),  $0.5 - 2$  (soft),  $2 - 8$  (hard),  $5 - 8$  (very-hard) and  $7.5 - 12 \text{ keV}$  (ultra-hard). All overlapping EPIC images are merged prior to source detection to increase the sensitivity to point sources. The detection algorithm is applied independently to each of the 5 spectral bands defined above.

The source detection is a two pass process. Source candidates are identified using the wavelet based EWAVELET source detection task of SAS at a low threshold of  $4\sigma$  above the background, where  $\sigma$  is the rms of the background counts. For each candidate source the Poisson probability of a random background fluctuation is estimated. This step involved the extraction of the total counts at the position of the source and the determination of the local background value. At each source position the counts are extracted within an elliptical aperture that corresponds to 70 per cent of the point spread function (PSF) encircled energy fraction (EEF), using the XMM EPIC PSF parametrisation of Georgakakis & Nandra (2011). The total counts at a candidate source position,  $T$ , is the sum of the extracted counts from individual EPIC cameras. For each source the local background is estimated by first masking out all detections within 4 arcmin of the source position using an elliptical aperture that corresponds to the 80 per cent EEF ellipse. The counts from individual EPIC cameras are then extracted using elliptical annuli centred on the source with inner and outer semi-major axes of 5 and 15 pixels (0.36 and 1.09 arcmin) respectively. The position angle and ellipticity of the ellipses are set equal to those of the 70 per cent EEF. The mean local background,  $B$ , is then estimated by summing up the background counts from individual EPIC cameras after scaling them down to the area of the source count extraction region. The Poisson probability  $P(T, B)$  that the extracted counts at the source position,  $T$ , are a random fluctuation of the background is calculated. We consider as sources the detections with  $P(T, B) < 4 \times 10^{-6}$ . The above methodology is optimised for the detection of point sources. Extended X-ray sources are also present in the catalogue but our method is not designed to identify them. For that we use the EMLDETECT task of SAS to perform PSF fits to the source count distribution and to estimate the source extent and the extent likelihood. EMLDETECT is applied separately to each of the five energy bands, soft, full, hard, very-hard and ultra-hard. The free parameters are the source count rate and source extent. The source positions are kept fixed during the minimization process. We consider as extended those sources with extension likelihood  $> 3$  in either the full or the soft spectral bands. The EMLDETECT task is also used to identify potential spurious sources in the catalogue. Point sources for which EMLDETECT failed to determine a reliable fit and hence, did not estimate

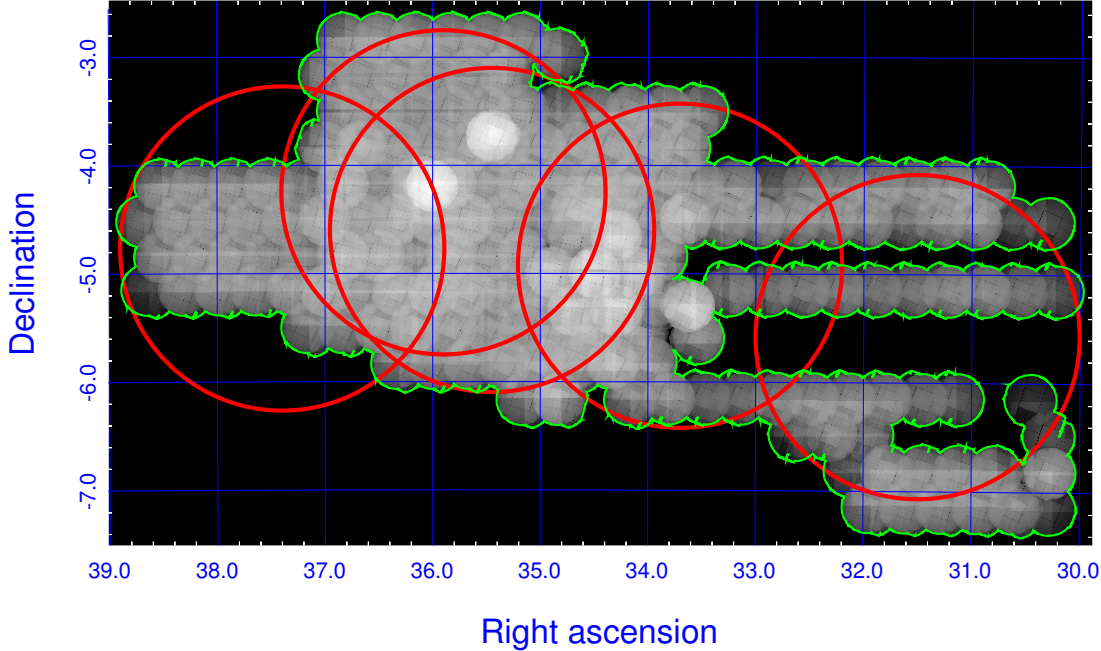


**Figure 1.** Layout of the XMM observations in the equatorial XMM-XXL field used in this paper. The distribution on sky coordinates of the EPIC PN+MOS exposure maps of individual XMM pointings is shown. The shading corresponds to different exposure times, with black being zero. The green line demarcates the limits of the area covered by the XMM data observed prior to 23 January 2012. XXL-N pointings observed after this date (total area of about  $5 \text{ deg}^2$ ) are not included in the analysis. This incompleteness in the X-ray data coverage is manifested by the dark (unexposed) horizontal stripes at e.g.  $\delta \approx -5.5 \text{ deg}$  and  $\alpha < 33.5 \text{ deg}$ . The red circles mark the positions of the five SDSS-III special spectroscopic plates used to target X-ray sources in the field. The size of each circle is 3 deg in diameter, the field-of-view of the SDSS spectroscopic plates.

a detection likelihood are marked as potentially spurious. In the final catalogue these sources are listed with a negative EMLDETECT detection likelihood.

The source catalogues in different energy bands are merged to produce a unique list of sources. A source detected in a particular energy band is cross-matched with sources in other energy bands by finding the closest counterpart. The search radius is set to the 70 per cent EEF circular radius. It should be stressed that our detection method is geared towards point sources and therefore the extended source catalogue should be treated with caution. Providing a well-defined sample of X-ray selected clusters is not among our goals.

The X-ray source positions suffer from systematic offsets because of pointing errors of the XMM-Newton telescope at the arcsec level (e.g. [Watson et al. 2009](#)). It is possible to correct for such systematic errors by cross-matching the X-ray source positions with external catalogues with higher astrometric accuracy. We use the EPOSCORR task of SAS to determine any systematic offsets in the astrometry of individual XMM observations by cross-correlating the X-ray source positions with optical sources in the SDSS-DR8 catalogue ([Aihara et al. 2011](#)) with magnitudes  $r < 22 \text{ mag}$ . The final astrometric accuracy of the X-ray source catalogue is  $1.5 \text{ arcsec}$  ( $1\sigma \text{ rms}$ ).

The flux of each source in different spectral bands is estimated by assuming a power-law X-ray spectrum with  $\Gamma = 1.4$ , i.e. similar to the XRB. The fluxes are corrected for Galactic absorption using the average Galactic hydrogen column density in the direc-

tion of each XMM observation based on the HI maps of [Kalberla et al. \(2005\)](#). The energy to flux conversion factors are such that the counts from the 0.5-2, 0.5-8, 2-8, 5-8 and 7.5-12 keV bands are transformed to fluxes in the 0.5-2, 0.5-10, 2-10, 5-10 and 7.5-12 keV bands respectively. The Bayesian methodology described by [Laird et al. \(2009\)](#) and [Georgakakis & Nandra \(2011\)](#) is adopted for the estimation of source fluxes and the corresponding  $1\sigma$  confidence intervals. The limiting 0.2 – 10 keV X-ray flux in the XXL-N is  $\sim 1.0 \times 10^{-15} \text{ erg s}^{-1} \text{ cm}^{-2}$ . Fig. 2 compares our fluxes in the 0.5-2 and 2-10 keV band with those in the XMM-LSS X-ray source catalogue ([Pierre et al. 2007](#)). A radius of 5 arcsec is used to match the XMM-LSS catalogue, which lead to a total of 3369 and 1098 common sources in the soft and hard bands, respectively. Overall there is good agreement, although at the faint-end our fluxes are systematically lower than the XMM-LSS ones. This is a direct consequence of the Bayesian approach of estimating fluxes, which accounts for Eddington bias as well as background and source count Poisson uncertainties. Taking these effects into account result in flux probability distribution functions that are skewed to low fluxes (see, [Laird et al. 2009](#); [Georgakakis & Nandra 2011](#)).

The construction of the sensitivity maps follows the methodology of [Georgakakis et al. \(2008\)](#). Fig. 3 plots the sensitivity maps in the 0.5-2, 2-10 keV, 0.5-10, and 5-10 keV energy bands. The construction of the X-ray number counts provides an independent consistency check of the overall data reduction process, including source detection, flux estimation and sensitivity map generation.



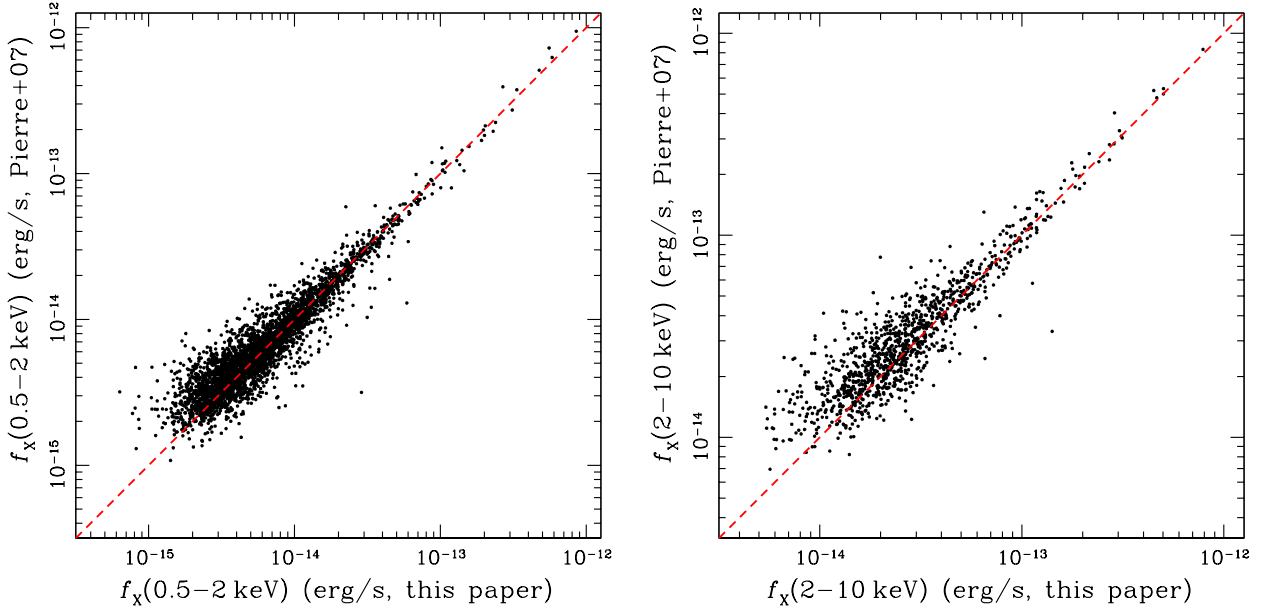


**Figure 2.** Comparison of the fluxes estimated in this paper with those in the XMM-LSS survey field (Pierre et al. 2015). We used a matching radius of 5 arcsec to match the two X-ray source catalogues. This results in a total of 3369 and 1098 common sources in the soft and hard bands respectively. Our fluxes are corrected for the different spectral index used in this paper ( $\Gamma = 1.4$ ) and (Pierre et al. 2007,  $\Gamma = 1.7$ ). There is fair agreement between the two studies. The systematic offset at the faint end is because of the Bayesian approach adopted here to determine fluxes.

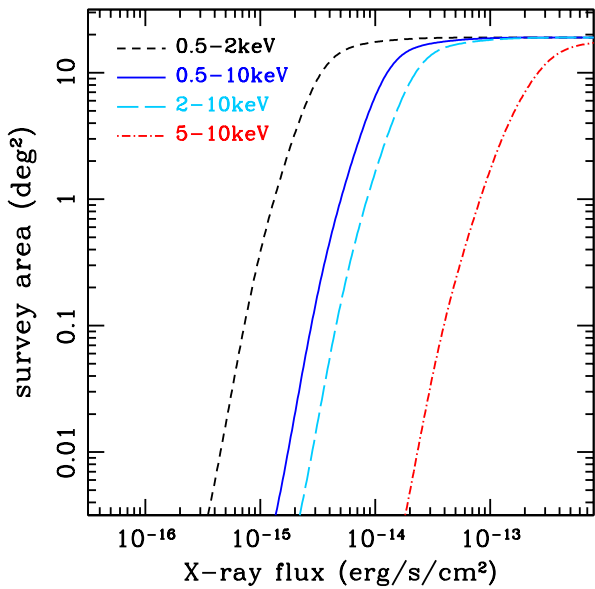


**Figure 3.** Sensitivity curves in the 0.5-2, 2-10, 0.5-10 and 5-10 keV spectral bands of the equatorial region of the XXL-N survey field.

Fig. 4 presents the differential X-ray number counts in the 0.5-2, 2-10 keV. For comparison that figure also plots the best-fitting differential count relations of Georgakakis et al. (2008) based on a combination of Chandra deep and shallow survey fields. There is encouraging agreement indicating that the X-ray source detection and sensitivity map generation are robust and consistent.

## 2.2 Extraction of X-ray spectra

The source spectra were extracted from circular source-centred regions, of which the radii were chosen to maximize the signal-to-noise over the 2-10 keV band via the SAS task EREGIONANALYSE. To select the background regions, we first masked out all the source regions in each image. In the case of the EPIC MOS camera, concentric annulus with inner radii of 40 arcsec and outer radii of 110 arcsec is selected if it is placed on the same CCD chip as the corresponding source. Otherwise, circular region of 90 arcsec radii, which is placed on the same CCD chip with roughly the same off-axis angle as the corresponding source, is selected. In the case of EPIC PN camera, the background events were extracted from source-free regions using circle of 90 arcsec radius at the same CCD read-out column as the corresponding source position. If this was not possible, e.g. the source might lie close to the CCD gaps, then a circle of 90 arcsec located at the same CCD chip was selected. X-ray events with pattern  $\leq 12$  for MOS camera and  $\leq 4$  for PN camera were used to extract the X-ray spectra. The redistribution matrix and ancillary file were generated using the SAS task RMFGEN and ARFGEN, respectively. For each source, to increase the S/N, the two MOS spectra in each observation were combined to form a single MOS spectrum if both the MOS1 and MOS2 spectra were available.

## 3 OPTICAL COUNTERPART IDENTIFICATION AND THE SOURCE CATALOGUE

In total, there are 8445 point-like X-ray sources detected in the XXL-N field. The source detection threshold is  $4\sigma$  above the background and the Poisson probability is less than  $4 \times 10^{-6}$  (see Section 2.1). In this section, we briefly describe the optical data anal-

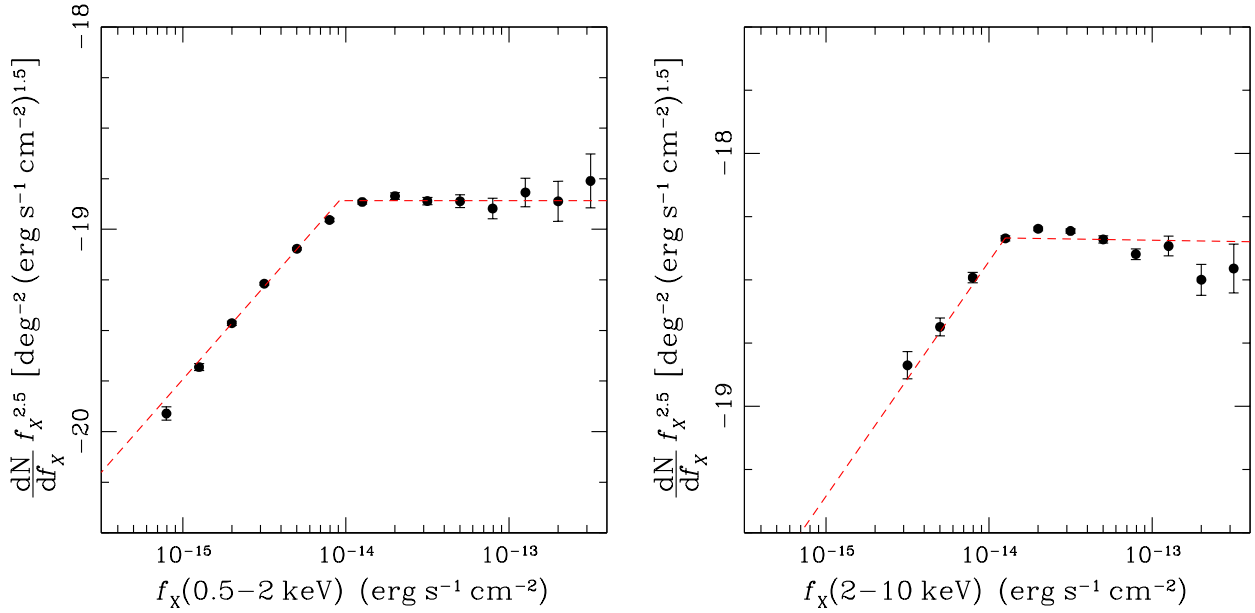


**Figure 4.** XXL-N differential number counts (black dots) normalized to the Euclidean slope in the 0.5-2 and 2-10 keV energy range. The (red) dashed line in each panel is the best-fitting relation estimated by [Georgakakis et al. \(2008\)](#) using a combination of deep and shallow survey fields.

ysis of the sources which have Sloan Digital Sky Survey (SDSS) observations (more details can be found in [Menzel et al. 2016](#)).

### 3.1 Cross-matching with optical data

X-ray sources in the XXL-N survey were matched to the SDSS-DR8 photometric catalogue ([Aihara et al. 2011](#)) following the Likelihood Ratio method ([Sutherland & Saunders 1992](#)) as implemented in [Georgakakis & Nandra \(2011\)](#). For the positional accuracy of the X-ray sources, we adopt a Gaussian distribution with a standard deviation of 1.5 arcsec (see above). A radius of 4 arcsec around the X-ray position is used to search for optical counterparts. We chose to use a likelihood threshold for secure counterparts  $LR_{\text{limit}} = 1.5$ . At this cut-off, 48 per cent (4075/8445) of the X-ray point sources have SDSS counterparts with an estimated spurious identification rate of about 6 per cent.

The full source catalogue is made available to the public <sup>2</sup> in FITS (Flexible Image Transport System) format. The information included in that file is listed in Appendix B.

### 3.2 Redshift measurements and optical classifications

Among the 8445 X-ray detected sources, a total of 3042 sources, in the optical magnitude range  $15.0 < r_{AB} < 22.5$ , were followed up by the BOSS spectrograph ([Menzel et al. 2016](#)). The redshift measurements as well as the optical classifications are extensively discussed in [Menzel et al. \(2016\)](#). Here we only outline the main procedures. The optical spectra are first analysed by the BOSS `spec1d` pipeline, which assigns a redshift and a classification using the  $\chi^2$ -minimization method ([Stoughton et al. 2002](#); [Bolton et](#)

[al. 2012](#)). However, the BOSS pipeline may fail to measure the redshift correctly for some sources, in particular for those of low signal to noise (S/N) or very high redshift (see [Menzel et al. 2016](#) for a list of reasons). Thus a dedicated *visual* inspection is applied to  $\sim 1200$  low S/N spectra in our data. At the end of the process, there are in total 2570 extragalactic sources which have reliable redshift measurements. Those sources are then classified based on their optical emission lines. Generally, the sources are classified as broad-line AGN (optical type-1) and narrow-line AGN (optical type-2) based on the full width at half maximum (FWHM) of their optical emission lines, i.e.  $H\beta$ , Mg II, C III] or C IV. In addition, sources that do not show any AGN-driven emission lines in their optical spectra are referred to as elusive AGN (eAGN). Sources are classified as BLAGN1 (or optical type-1) if one of the optical lines have FWHM larger than  $1000 \text{ km s}^{-1}$ . NLAGN2 (or optical type-2) are objects with FWHMs of all the  $H\beta$ , Mg II, C III] or C IV emission lines less than  $1000 \text{ km s}^{-1}$ . However, in some cases, due to strong host galaxy continuum contribution or very low S/N ratio spectra, the optical emission lines of some sources are not significantly detected. These objects are defined as NLAGN2cand. The elusive AGN are further classified as eAGN-ALG and eAGN-SFG depending on their optical spectral properties. The eAGN-ALG are sources whose optical spectra show absorption lines and a few narrow emission lines which are not significant, while eAGN-SFG are objects with optical emission lines from young stars. In this work, the optical type-2 AGN include all the NLAGN2, NLAGN2cand and the elusive AGN. In total, we have 1787 type-1 AGN (70 per cent), 726 type-2 AGN (28 per cent, NLAGN2: 10 per cent, NLAGN2cand: 11 per cent, eAGN-SFG: 3 per cent, eAGN-ALG: 4 per cent). The remaining 57 sources (2 per cent) cannot be reliably classified due to the low S/N of their optical spectra. The fraction of different types of sources in our sample can be found in Table 1.

<sup>2</sup> [http://www.mpe.mpg.de/XraySurveys/XMM-XXL/XMM-XXL/ADD-ONS/Xray\\_data/xxl\\_xray\\_detected\\_source\\_2016MAR30.fits](http://www.mpe.mpg.de/XraySurveys/XMM-XXL/XMM-XXL/ADD-ONS/Xray_data/xxl_xray_detected_source_2016MAR30.fits)

**Table 1.** The fraction of different types of sources in our spectroscopic AGN sample. Sources are classified as BLAGN1 (or optical type-1) if one of the optical lines, i.e.  $H\beta$ , Mg II, C III] or C IV, have FWHM larger than  $1000 \text{ km s}^{-1}$ . NLAGN2 (or optical type-2) are objects with FWHMs of all optical emission lines less than  $1000 \text{ km s}^{-1}$ . Objects with no significantly detected optical emission lines are defined as NLAGN2cand. The eAGN-ALG are sources whose optical spectra show absorption lines and a few narrow emission lines which are not significant, while eAGN-SFG are objects with optical emission lines from young stars. The remaining sources (defined as unknown) cannot be reliably classified due to the low S/N of their optical spectra.

Classification	Optical type-1		Optical type-2			Unknown
	BLAGN1	NLAGN2	NLAGN2cand	eAGN-SFG	eAGN-ALG	
Fractions	0.70	0.10	0.11	0.03	0.04	0.02

### 3.3 $M_{\text{BH}}$ estimation

To estimate single-epoch virial BH masses from continuum luminosities and broad-line widths (e.g. Shen 2013), we perform spectral fits to the BOSS spectroscopy of the type-1 objects in our sample. The spectral fitting procedure is similar to the global fitting scheme described in Shen & Liu (2012). We fit a global pseudo-continuum model (including a power-law component, broad Fe II emission, and a low-order polynomial to account for spectral curvature due to reddening) to several continuum windows free of major emission lines (other than the copious Fe II emission). For the UV Fe II template, we use the Vestergaard & Wilkes (2001) template (1000 – 2200 Å), and the modified template by Salviander et al. (2007) for the Mg II region (2200 – 3090 Å); we augment the 3090 – 3500 Å region using the template derived by Tsuzuki et al. (2006). For the optical Fe II template (3686 – 7484 Å) we use the one provided by Boroson & Green (1992).

The best-fitting pseudo-continuum model is subtracted from the spectrum, leaving the emission-line-only spectrum. We then fit the several major broad lines (e.g.,  $H\beta$ , Mg II, C IV) that are commonly used for single-epoch virial BH mass estimators with multiple Gaussians (in logarithmic wavelength space). The details of the fitting parameters and constraints can be found in Shen & Liu (2012). We estimate the continuum luminosities and the broad-line FWHMs from the model fits. Finally, we use a Monte Carlo method to estimate the uncertainties in the measured spectral quantities (e.g. Shen et al. 2008, 2011), in which we perturb the original spectrum with the reported flux density errors, and repeat the same fitting procedure on 50 trials of mock spectra. The  $1\sigma$  errors on the measured spectral quantities are estimated as the semi-amplitude of the range defined by the 16 per cent and 84 per cent percentiles in the distribution from the 50 trials.

With the measured continuum luminosities and broad-line FWHMs, we use several single-epoch virial mass estimators to estimate BH masses. The fiducial mass recipes we adopt are:  $H\beta$  at  $z < 0.9$  Vestergaard & Peterson (2006); Mg II at  $0.9 < z < 2.2$  (Shen et al. 2011); C IV at  $z > 2.2$  (Vestergaard & Peterson 2006). These redshift divisions differ slightly from Shen et al. (2011) for DR7 quasars, given the slight difference in the spectral coverage between SDSS-I/II and SDSS-III.

The measurement errors on these virial BH masses are propagated from measurement errors in continuum luminosity and broad-line FWHM, which could be substantial for noisy spectrum. In addition, there is a substantial systematic uncertainty of  $\sim 0.4 - 0.5$  dex in these single-epoch virial BH masses (see extensive discussions in Shen 2013), and we caution on the consequences of the large systematic uncertainties in these BH mass estimates. The distribution of the  $M_{\text{BH}}$  is shown in the top panel (black empty

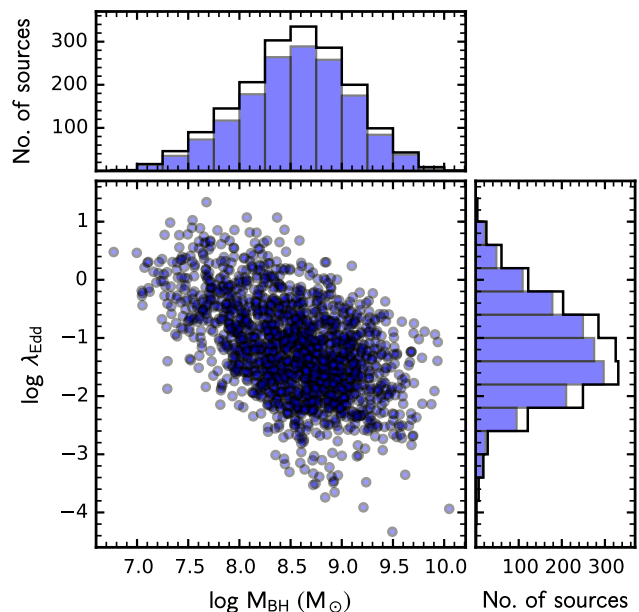


**Figure 5.** The central panel shows the distribution in the  $\log M_{\text{BH}} - \log \lambda_{\text{Edd}}$  of the 1787 type-1 sources in the spectroscopic sample. The black empty histograms in the top and right panels show the distributions of the  $\log M_{\text{BH}}$  and  $\log \lambda_{\text{Edd}}$  for all the type-1 AGN, respectively. The blue filled histograms are for the type-1 AGN sample used in the X-ray spectral stacking (see Section 5).

histogram, the blue filled histograms are for the type-1 AGN sample used in the X-ray spectral stacking, see Section 5) of Fig. 5.

Comparisons of SE BH masses using different emission lines have been performed in several previous studies (e.g., Shen et al. 2008, 2011; Shen & Liu 2012, Shen 2013 and references therein). These studies revealed that SE BH masses estimates using different emission lines, when adopting the fiducial SE mass formula, are generally consistent with each other with negligible systematic offsets and scatters that are lower than the systematic uncertainties of these mass estimates. This ensures there is no systematic bias in using different lines to estimate BH masses at different redshifts in this study. As shown in Fig. 6 (left:  $M_{\text{BH}}$  calculated using Mg II against  $M_{\text{BH}}$  obtained using  $H\beta$ , right:  $M_{\text{BH}}$  estimated using C IV against  $M_{\text{BH}}$  obtained using Mg II), our results are generally in agreement with previous studies. The large scatter found in Fig. 6 is mainly due to the low S/N of the data, especially for the correlation between the BH mass estimated with  $H\beta$  and Mg II. This is clearly illustrated in the left panel of Fig. 6. The  $M_{\text{BH}}(H\beta)$  is consistent with the BH mass obtained using Mg II if we limit the data

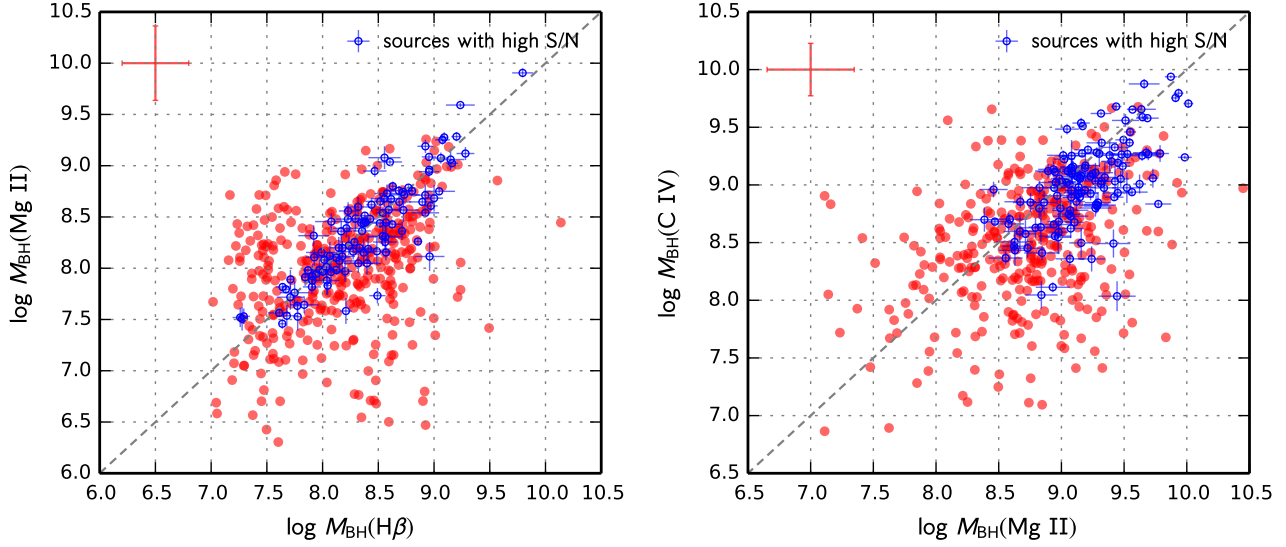


**Figure 6.** Left: comparison of  $M_{\text{BH}}$  estimated using Mg II to  $M_{\text{BH}}$  obtained using  $H\beta$ . Right:  $M_{\text{BH}}$  calculated using C IV against  $M_{\text{BH}}$  obtained using Mg II. Blue circles with error bars are sources with higher S/N, i.e. the uncertainties of the measured  $M_{\text{BH}}$  are less than 0.15. The remaining sources with lower S/N are indicated with red points. The  $M_{\text{BH}}$  of these sources have uncertainties of  $\sim 0.3 - 0.4$  dexs, as shown by the typical error bars in the upper-left of each panel.

to sources with high S/N. However, as shown in the right panel of Fig. 6, the scatter is still large even for sources have well determined Mg II- and C IV-based BH mass estimations. Previous studies have also shown that the C IV-based BH mass estimates have a larger scatter around  $H\beta$ -based mass estimates than that for Mg II. We thus note that C IV may be a less reliable line in estimating BH masses compared to  $H\beta$  and Mg II (see discussion in Shen 2013).

#### 4 PROPERTIES OF AGN WITH REDSHIFT MEASUREMENTS

##### 4.1 X-ray properties

In this work, a total of 2512<sup>3</sup> sources, which have reliable redshift measurements and optical classifications, are used to study the X-ray properties of AGN in the XXL-N. The background-subtracted rest-frame 2 – 10 keV photon counts distribution of the sources in our sample is shown in Fig. 7 (blue for PN and red for MOS). We adopted the Bayesian X-ray Analysis software (BXA, Buchner et al. 2014) to analyse the X-ray spectrum of each individual source. The detail methodology of the Bayesian approach is present in Buchner et al. (2014). The best model for describing the X-ray spectra of a large sample of AGN found in that paper, i.e. is used to fit the X-ray spectra of the sources in our sample. This model consists of three main components: a) the BNTORUS model (Brightman & Nandra 2011), which includes an intrinsic power-law component modified by photoelectric absorption and Compton scattering from absorption material with toroidal geometry, is used to model the power-law continuum as well as the absorption and Compton scattering feature observed in X-ray spectra of AGN; b) the PEXMON model (Nandra et al. 2007) is included to account for the reflection component which is also absorbed by the same

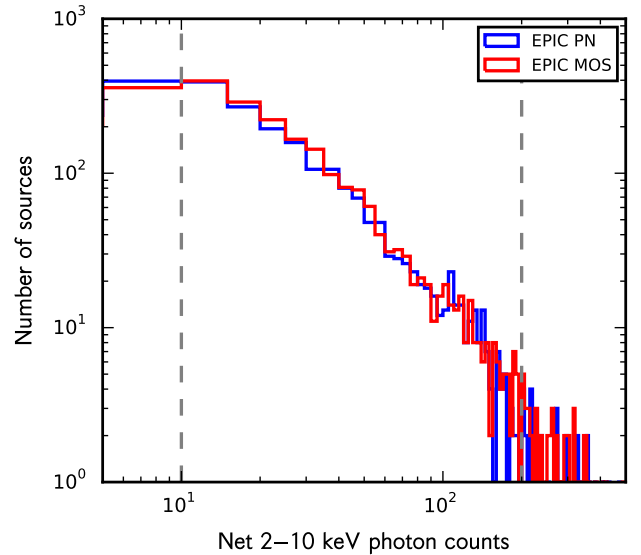


**Figure 7.** Distribution of the rest-frame 2-10 keV net photon counts for the all the sources which have reliable redshift measurements. The vertical dashed lines indicate the photon count boundaries of the AGN sample presented in the Section 5.

material as the intrinsic power-law continuum; c) a soft scattering component, which is approximated with an unabsorbed power-law, is also added to model the soft X-ray excess (soft scattering) found in type-1 (type-2) AGN. The opening angle and the inclination of the BNTORUS model are fixed at  $45^\circ$  and  $85^\circ$ , respectively. The photon index of the PEXMON model, as well as the scattering components, are linked to the power-law component in the BNTORUS model. The inclination parameter in the PEXMON model is fixed at  $60^\circ$ . The normalization of this component is modelled relative to that of the BNTORUS model and is allowed to vary between 0.1 and

<sup>3</sup> Due to calibration issues, one source (UXID: N.121.7) is excluded from the X-ray analysis.



100. The same is applied to the normalization of the soft scattering component, but with an upper limit of 0.1 and a lower limit of  $10^{-9}$ .

Liu & Li (2015) have recently shown that the BNTORUS model will over predict the soft-X-ray emission in heavily obscured objects, comparing with the results obtained from the MYTORUS model (Murphy & Yaqoob 2009) and the model built by Liu & Li (2014). Using the data observed with the *Nuclear Spectroscopic Telescope Array* (*NuStar* Harrison et al. 2013), there have been many studies that fit the spectra with both MYTORUS and BNTORUS models. They found no evidence that one model gives significantly different parameters than the other, except for sources with  $N_{\text{H}}$  higher than  $10^{25} \text{ cm}^{-2}$  or extreme opening angles found with BNTORUS (e.g. Bauer et al. 2015; Arévalo et al. 2014). Brightman et al. (2015) also conducted comparisons of MYTORUS and PEXRAV (Magdziarz & Zdziarski 1995) models with BNTORUS using a sample of AGN observed by *NuStar*. They again found that the parameters given by the two models are consistent with each other, when both models are valid. The reason for the agreement, despite the differing reflection strength predicted by MYTORUS and BNTORUS, is that the difference is only large in the softer energies where typically scattered/thermal emission dominates over the reflection. In this work, the majority of the sources in the AGN sample have column density less than  $10^{25} \text{ cm}^{-2}$  (see below) and a soft scattering component is included to model the scattered emission for heavily obscured objects, thus the BNTORUS model is still appropriate.

We jointly fit the PN and MOS spectra for each source, if both are available. A MOS/PN normalization factor is thus included to allow the normalization of the MOS spectra to vary. We have in total 6 free parameters, the photon index  $\Gamma$  of the intrinsic power-law, the column density  $N_{\text{H}}$ , the MOS/PN normalization factor, the normalization of the torus, Compton reflection and scattering components. To apply the BXA method, priors need to be assigned for each of these parameters. Following Buchner et al. (2014), we applied log-uniform priors on all normalization and column density parameters, while Gaussian priors are used for the photon index  $\Gamma$  (with the mean of 1.95 and standard deviation of 0.15) and the MOS/PN normalization factor (with the mean of 1.0 and standard deviation of 0.25 based on the results of a simple power-law fitting) parameters. In addition, models for the *XMM-Newton* EPIC PN and MOS background spectra constructed by Maggi et al. (2014), which include an empirical instrumental background component developed by Sturm (2012) and astrophysical background component of Kuntz & Snowden (2010), are adopted in order to apply the BXA method.

The spectra are fitted in the observed 0.5 – 8 keV energy range. Hereafter the quoted value of each parameter is the median of its posterior distribution unless specified otherwise. As shown in Fig. 8, the distribution of the photon index parameter has a similar shape as the input priors, though the mean photon indices for both type-1 and type-2 AGN ( $\Gamma \sim 2.0$ ) are higher than the mean of the Gaussian prior. The standard deviations of the photon index are also peaked at values close to  $\sim 0.15$  (see the inset in Fig. 8). This may be an indication that the posterior distributions of the photon index are driven by the priors. To test this, the photon index posteriors are re-analysed under a flat prior, using the methodology described in Buchner et al. (2015, see their Appendix A). We find that, assuming a flat prior, the intrinsic distribution of the posteriors can be well described by a Gaussian of mean 2.14 (2.10) and standard deviation 0.22 (0.33) for type-1 (type-2) AGN, consistent with the result obtained by assuming a Gaussian prior. Thus, the result shown in Fig. 8 is *not* driven by the prior, and is robust against the

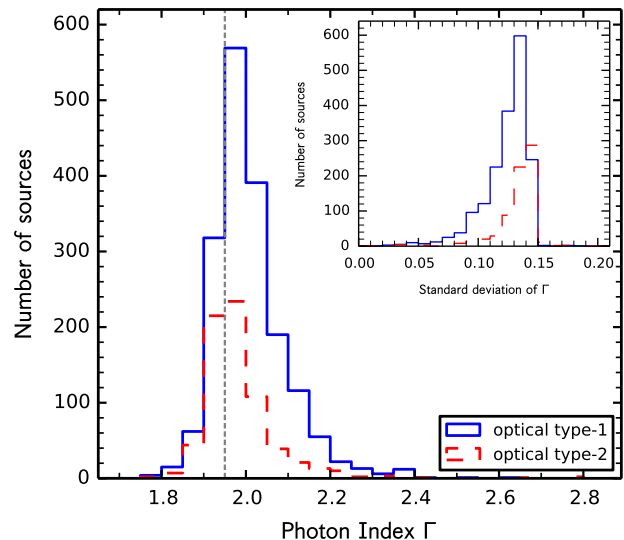


**Figure 8.** Distribution of photon index for type-1 (solid blue) and type-2 (dashed red) AGN. For each of the source, the median value of the posterior distribution is used. The mean value,  $\Gamma = 1.95$ , for the photon index prior is indicated with vertical dashed line. Inset: Distribution of the standard deviation of  $\Gamma$  for type-1 (solid blue) and type-2 (dashed red) AGN.

choice of prior. The asymmetry of the photon index distribution is due to sources which have very soft and steep X-ray spectra, e.g. sources with strong soft X-ray excess.

For the rest of the parameters with log-uniform priors and the MOS/PN normalization factor parameter, though with large uncertainties, the fitted values also provide interesting information (see Section 6.4). Fig. 9 shows the distributions of the column density for sources with more than 10 photon counts in either the PN or MOS spectra (blue: type-1 AGN; red: type-2 AGN). The cumulative  $N_{\text{H}}$  distribution of type-1 AGN (blue curve, fraction of sources with column density *smaller* than a given value) and the reversed cumulative  $N_{\text{H}}$  distribution of type-2 AGN (red curve, the fraction of sources with column density *larger* than a given value) are also shown in Fig. 9. The full posterior distribution of the column density parameter is used to generate this plot. Generally, the optically selected type-2 AGN have a different distribution from the type-1 AGN, i.e. with more sources having column density higher than  $10^{22} \text{ cm}^{-2}$ . It also clearly shows that  $\sim 40$  per cent of type-1 (type-2) AGN have X-ray measured line of sight column density larger (lower) than  $10^{21} \text{ cm}^{-2}$ . Our results, with a larger spectroscopic AGN sample, it is consistent with the conclusion found in Merloni et al. (2014, see also Trouille et al. 2009) using an AGN sample selected from the *XMM-COSMOS* survey, though with a slightly smaller intersection value (i.e.  $\sim 10^{20.9} \text{ cm}^{-2}$  in our sample and  $\sim 10^{21.1} \text{ cm}^{-2}$  in their spectroscopic sample) of the two cumulative distribution.

To derive the rest-frame 2 – 10 keV intrinsic X-ray luminosity distribution, both the Galactic and host galaxy column densities are fixed at zero. The posterior distribution for the X-ray luminosity of each source is then calculated using the BNTORUS+PEXMON+SCATTERING model. Fig. 10 shows the distribution of the sources in the  $\log L_{2-10\text{keV}} - z$  plane for type-1 (blue points) and type-2 (red stars) AGN.

The median values of the posterior distributions for the parameters are included in Table 2. In Table 2, we also present the

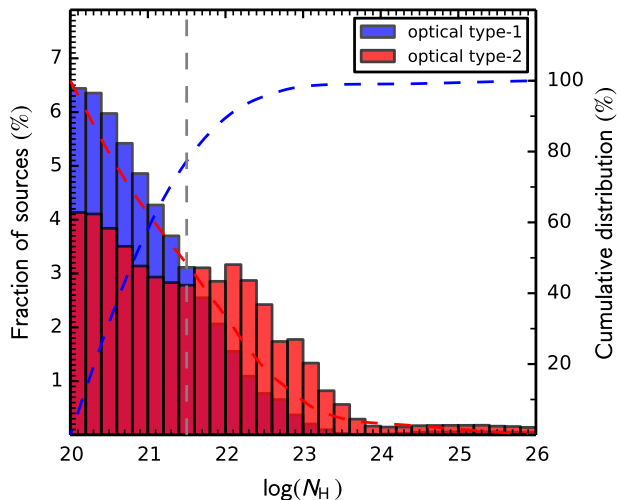


**Figure 9.** Normalized distribution of the column density parameter for sources with photon counts larger than 10 in either the PN or MOS spectra. For each source, the full posterior distribution is used. Optical classified type-1 and type-2 AGN are shown in blue and red histogram, respectively. The blue dashed line shows the cumulative distribution  $C(\log N_{\text{H}})$  for type-1 AGN and the red dashed line shows the negative cumulative distribution  $1 - C(\log N_{\text{H}})$  for type-2 AGN. The vertical dashed line indicates the  $\log N_{\text{H}}$  value we used to define the X-ray obscured/unobscured samples (see Section 6.4).

redshift, optical classification,  $L_{2-10\text{keV}}$  as well as the rest-frame 2-10 keV net photon counts for each source. The full table can be found online, in which the 3rd, 16th, 84th and 97th percentiles of each parameter are also included.

#### 4.2 Bolometric luminosity and Eddington ratio estimation for type-1 AGN

The bolometric luminosity  $L_{\text{bol}}$  can be best determined by integrating the spectral energy distribution (SED) of an AGN (e.g. Elvis et al. 1994; Richards et al. 2006). In this work, only the radiation directly produced by the accretion process, i.e. the optical/UV thermal emission from the accretion disc and the hard X-ray radiation produced by inverse-Compton scattering of the soft disc photons by a hot corona, are included to estimate  $L_{\text{bol}}$ , i.e.  $L_{\text{bol}} = L_{\text{disc}} + L_{2-10\text{keV}}$ . The infrared (IR) radiation, which is known to be reprocessed UV radiation (Antonucci 1993), is excluded.

The calculation of the hard X-ray radiation  $L_{2-10\text{keV}}$  for each source is described in Section 4.1. To estimate  $L_{\text{disc}}$ , we assume that the optical/UV emission are originated from a standard thin accretion disc (AD Shakura & Sunyaev 1973). In the AD model, the flux of per unit area is

$$F = \frac{3}{8\pi} \frac{GMM_{\text{BH}}}{R^3} f_c(r, a) \quad (1)$$

where  $R$  is the radius and  $f_c(r, a)$  is a dimensionless factor depending on black hole spin ( $a$ ) and dimensionless radius  $r = R/R_{\text{g}}$  ( $R_{\text{g}} = GM/c^2$ , gravitational radius). The  $f_c(r, a)$  factor is ignored since only the radiation from relatively large radii is considered. It is clear from Equation 1 that the full disc spectrum is determined by the BH mass  $M_{\text{BH}}$  and the accretion rate  $\dot{M}$ . We estimate the  $M_{\text{BH}}$

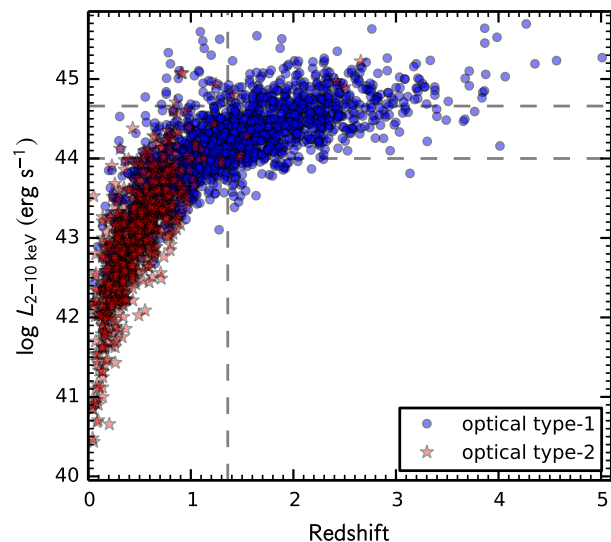


**Figure 10.** Distribution of sources in the rest-frame intrinsic 2-10 keV luminosity-redshift plane for type-1 (blue points) and type-2 (red stars) AGN. The luminosity and redshift boundaries for the type-1 redshift-luminosity sub-samples (see Section 5.1) are indicated by the vertical and horizontal dashed lines.

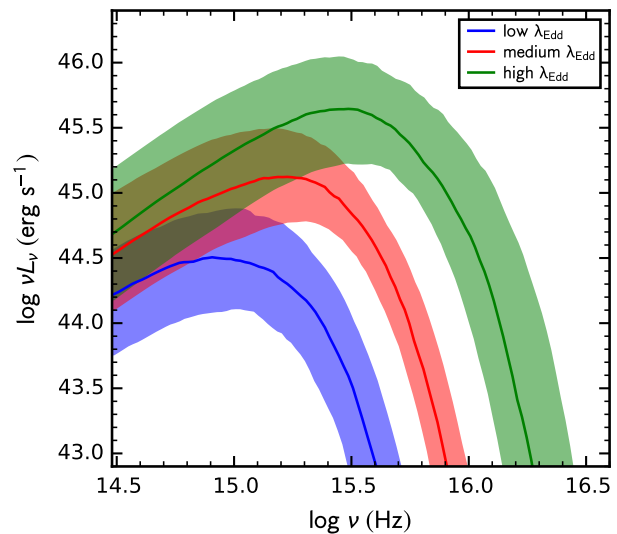


**Figure 11.** The median SED for the three different  $\lambda_{\text{Edd}}$  samples (see Section 5.1). The filled area marked the 25th and 75th percentile range.

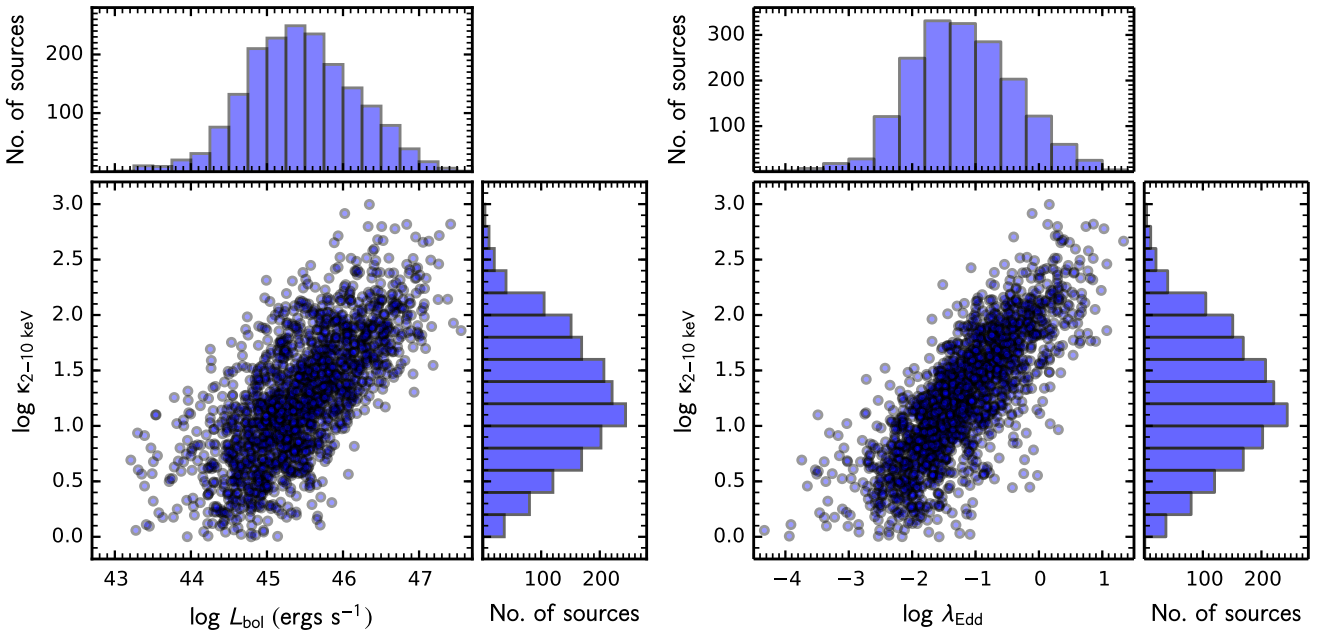
from the optical broad lines as discussed in Section 3.3. The accretion rate  $\dot{M}$  is calculated from the empirical relation between the  $\dot{M}$ , the  $M_{\text{BH}}$  and the optical monochromatic luminosity at 4681 Å ( $L_{\text{opt},45}$ ) presented in Davis & Laor (2011, see their equation 8). To calculate the  $L_{\text{opt},45}$ , we assume a power-law form for the optical continua, i.e.,  $f(\lambda) \propto \lambda^{-\alpha_\lambda}$ , where the index  $\alpha_\lambda$  is calculated from the measured  $L_{3000}$  and  $L_{5100}$  if both are available, or assuming  $\alpha_\lambda = 1.5$  if only one of them is available or only monochromatic luminosities measured at the other wavelength are available.

At a certain radius, the effective temperature  $T_{\text{eff}}$  of the disc is  $T_{\text{eff}} = (F/\sigma)^{1/4}$ , assuming that the disc emits locally as black-

**Table 2.** Properties of sources with reliable redshift measurement and optical classification

UXID (1)	$z$ (2)	classification (3)	$N_{\text{H}}$ (4)	$\Gamma$ (5)	normalization (6)	reflection component (7)	soft scattering (8)	$L_{2-10\text{keV}}$ (9)	cts PN (10)	cts MOS (11)
N_14_52	2.704	BLAGN1	21.10	1.98	-5.04	-0.10	-4.14	44.61	11	5
N_12_26	2.471	BLAGN1	20.88	1.96	-5.08	-0.16	-3.92	44.52	14	22
N_13_30	2.405	BLAGN1	20.97	1.98	-4.66	-0.30	-3.88	44.89	56	46
N_12_35	2.209	BLAGN1	20.74	2.08	-4.84	-0.35	-4.08	44.58	24	10
N_59_18	2.921	BLAGN1	20.88	2.01	-4.87	-0.31	-3.93	44.80	21	30

The columns are: (1) unique ID for each source; (2) redshift; (3) optical classification (4) logarithmic median value of the  $N_{\text{H}}$  parameter, in units of  $\text{cm}^{-2}$ ; (5) median value of the photon index parameters; (6) logarithmic median value of the normalization; (7) logarithmic median value of the reflection component normalization; (8) logarithmic median value of the soft scattering normalization; (9) logarithmic median value of the 2-10 keV luminosity in units of  $\text{erg s}^{-1}$ ; (10) rest-frame 2-10 keV photon counts of the PN spectrum; (11) rest-frame 2-10 keV photon counts of the MOS spectrum. The full table is available online.


**Figure 12.** Left: The main panel shows the distribution of the sources in the  $\kappa_{2-10\text{keV}} - L_{\text{bol}}$  plane (blue points). The top panel and right panel show the distribution of the  $L_{\text{bol}}$  and  $\kappa_{2-10\text{keV}}$  for the sources in the sample, respectively. Right: the same as the left plot, but for the  $\kappa_{2-10\text{keV}}$  versus  $\lambda_{\text{Edd}}$ .

body. To calculate the disc luminosity  $L_{\text{disc}}$ , we then integrated it over the disc surface with inner radius  $R_{\text{in}} = 20R_{\text{g}}$  and outer radius  $R_{\text{out}} = 6000R_{\text{g}}$  in the  $3.0 \times 10^{14} - 4.8 \times 10^{17}$  Hz frequencies range. As an illustration, we show the median SED of the three different  $\lambda_{\text{Edd}}$  samples (see Section 5.1) in Fig. 11. This shows that, on average, the accretion disc becomes more luminous and hotter with increasing  $\lambda_{\text{Edd}}$ .

The bolometric luminosity is then computed as the sum of the disc luminosity and the 2 – 10 keV X-ray luminosity. The  $\lambda_{\text{Edd}}$ , given by  $\lambda_{\text{Edd}} = L_{\text{bol}}/L_{\text{Edd}}$ , as a function of the  $M_{\text{BH}}$  is plotted on the central panel of Fig. 5, while the  $\lambda_{\text{Edd}}$  distribution is shown in the horizontal histogram. Fig. 12 shows the 2 – 10 keV X-ray bolometric correction ( $\kappa_{2-10\text{keV}} = L_{\text{bol}}/L_{2-10\text{keV}}$ ) versus  $L_{\text{bol}}$  (left panel) and the  $\lambda_{\text{Edd}}$  (right panel). Tight correlations between the  $\kappa_{2-10\text{keV}}$  and  $L_{\text{bol}}$  (Pearson correlation coefficient  $r = 0.71$ ) as well as the  $\lambda_{\text{Edd}}$  (Pearson correlation coefficient  $r = 0.78$ ) are found in our sample as clearly shown in Fig. 12. A similar trend, that the sources with higher bolometric luminosities have higher bolometric corrections, was found in Lusso et al. (2012). A relation between

the  $\kappa_{2-10\text{keV}}$  and  $\lambda_{\text{Edd}}$  is also found in several previous works (Vasudevan & Fabian 2007, 2009; Vasudevan et al. 2009; Lusso et al. 2012). The tight  $\kappa_{2-10\text{keV}} - L_{\text{bol}}$  relation shown in Fig. 12 as well as the correlation between  $\kappa_{2-10\text{keV}}$  and  $\lambda_{\text{Edd}}$ , rather than intrinsic, can however be a natural outcome of our flux-limited sample, which will lead to a correlation between the monochromatic optical luminosity  $L_{\text{mon,opt}}$  and the X-ray luminosity  $L_{2-10\text{keV}}$ . We tested the significance of the correlation by means of simulations. We generated a sample which the  $\log N - \log S$  of both the X-ray and optical flux follows a power-law form, and has a redshift distribution similar to our AGN sample. We then applied the flux cut-off,  $f_{0.5-10\text{keV}} > 1 \times 10^{-15} \text{ erg s}^{-1} \text{ cm}^{-2}$  and  $R_{4681} < 22 \text{ mag}$ , on the simulated sources. Using the  $L_{\text{mon,opt}}$  and  $L_{2-10\text{keV}}$  of the simulated data we obtain a Pearson correlation coefficient value  $r$  of  $\sim 0.57$ , which is smaller than the correlation coefficient found in the observed data ( $r \sim 0.71$ ). Thus the observed correlations in our sample should not be purely due to the selection bias. This result is also consistent with the conclusion that the strong correlation between the monochromatic UV luminosity at 2500Å and the

**Table 3.** The optical properties of the type-1 AGN in our sample

UXID (1)	$z$ (2)	$\log M_{\text{BH}}$ (3)	$\log L_{1350}$ (4)	$\log L_{1700}$ (5)	$\log L_{3000}$ (6)	$\log L_{5100}$ (7)	$\log L_{\text{disc}}$ (8)	$\log L_{\text{bol}}$ (9)	$\log \lambda_{\text{Edd}}$ (10)
N.0.16	1.597	8.10	—	44.85	44.84	—	45.81	45.83	-0.39
N.0.27	1.741	8.82	44.60	44.66	44.97	—	45.31	45.36	-1.58
N.0.29	0.996	7.73	—	—	44.32	44.47	45.70	45.70	-0.15
N.0.30	1.687	9.68	45.70	45.64	45.57	—	45.31	45.49	-2.30
N.0.32	0.985	8.11	—	—	44.13	44.34	45.14	45.16	-1.06

The columns are: (1) unique ID for each source; (2) redshift; (3)  $M_{\text{BH}}$  estimate using method described in Section 3.3; (4)-(7) optical monochromatic luminosity in units of  $\text{erg s}^{-1}$ ; (8) the disc luminosity is calculated with the method presented in Section 4.2; (9) the bolometric luminosity in units of  $\text{erg s}^{-1}$ ; (10)  $\lambda_{\text{Edd}}$ . The full table is available online.

X-ray luminosity at 2 keV is independent of redshift (Risaliti & Lusso 2015). The distributions of the  $L_{\text{bol}}$  and  $\kappa_{2-10\text{keV}}$  are shown in Fig. 12 (top panel:  $L_{\text{bol}}$ , right panel:  $\kappa_{2-10\text{keV}}$ ). The  $\kappa_{2-10\text{keV}}$  found in our sample, with a mean value of  $\sim 18$ , are consistent with the values found in previous works (e.g. Vasudevan & Fabian 2007; Lusso et al. 2012).

The optical spectral properties of the type-1 AGN as well as the estimated  $M_{\text{BH}}$ ,  $L_{\text{bol}}$  and  $\lambda_{\text{Edd}}$  are included in Table 3 (the full table is available online). The optical monochromatic luminosities are estimated via spectral fitting procedure described in Section 3.3.

## 5 X-RAY SPECTRAL STACKING OF THE TYPE-1 AGN

As shown in Fig. 7, the majority of the sources in our sample have low photon counts. Spectral stacking is an effective way to obtain a composite spectrum with high S/N in this case. Here we adopted the rest-frame X-ray spectral stacking method to investigate the average properties of AGN.

We studied various type-1 AGN sub-samples selected on the basis of their physical properties, such as the X-ray luminosity, redshift,  $\lambda_{\text{Edd}}$  as well as  $M_{\text{BH}}$ . For each source the PN or MOS spectra is used if a) the rest-frame 2-10 keV photon counts is larger than 10 and less than 200; b) the fitted MOS/PN normalization factor is in the range 0.5-1.5 so that we can reject poor quality spectra and sources for which one of the spectra fall, for example, at the edge or in the gap between CCDs. About 10 per cent of the total type-1 sources are discarded after applying these criteria. The rest of the sources form the main sample for the X-ray spectral stacking. The median redshift and  $L_{2-10\text{keV}}$  of this main sample are 0.87 and  $3.1 \times 10^{44} \text{ erg s}^{-1}$ , respectively.

### 5.1 Sub-samples

We first define four redshift-luminosity sub-samples. The sub-samples are selected in a way that the stacked spectra have similar S/N. The main sample is divided into two redshift bins, the low-redshift bin including sources with redshift  $z < 1.36$  and the high-redshift bin with  $z > 1.36$ . Each redshift bin is further split into two X-ray luminosity bins: low ( $42.00 < \log L_{2-10\text{keV}} < 44.00 \text{ erg s}^{-1}$ ) and medium ( $44.00 < \log L_{2-10\text{keV}} < 44.66 \text{ erg s}^{-1}$ ) luminosity subsets for the low redshift bin, medium ( $44.00 < \log L_{2-10\text{keV}} < 44.66 \text{ erg s}^{-1}$ ) and high ( $44.66 < \log L_{2-10\text{keV}} < 46.00 \text{ erg s}^{-1}$ ) luminosity subsets for the high redshift bin. Thus, in total, we have four luminosity-redshift sub-samples, namely: low-redshift low-luminosity (LL), low-redshift medium luminosity (LM), high-redshift medium luminosity (HM) and high-redshift high luminosity (HH) sub-samples. The details of each sub-sample are shown in Table 4, and illustrated in Fig 10.

**Table 4.** Properties of the type-1 AGN sub-samples

Sample	$\bar{z}$ (1)	$\bar{L}_{2-10 \text{ keV}}$ (2)	$\bar{M}_{\text{BH}}$ (3)	$\bar{\lambda}_{\text{Edd}}$ (4)	#src (5)	#spec (6)	cts (7)
LL	0.77	43.67	8.22	-1.41	418	708	25581
LM	1.14	44.21	8.57	-1.50	270	500	25367
HM	1.82	44.39	8.71	-1.20	517	858	24660
HH	2.25	44.82	8.97	-0.87	256	461	24717
Low Edd	1.24	44.13	8.81	-2.00	481	826	34191
Med Edd	1.44	44.28	8.63	-1.29	496	863	34985
Hig Edd	1.67	44.33	8.25	-0.44	557	949	35271
Low MBH	1.11	43.98	8.07	-0.74	576	973	36008
Med MBH	1.42	44.24	8.64	-1.41	548	936	36320
Hig MBH	1.77	44.54	9.12	-1.59	410	729	32119

The columns are: (1) median redshift; (2) median 2-10 keV luminosity in unit  $\text{erg s}^{-1}$ ; (3) median  $M_{\text{BH}}$ ; (4) median  $\lambda_{\text{Edd}}$ ; (5) number of sources; (6) number of spectra, PN and MOS spectra are counted independently; (7) total 2-10 keV net photon counts

ity (HH) sub-samples. The details of each sub-sample are shown in Table 4, and illustrated in Fig 10.

We also define three  $M_{\text{BH}}$  sub-samples, namely: low  $M_{\text{BH}}$  sample with  $\log M_{\text{BH}} < 8.4$ ; medium  $M_{\text{BH}}$  with  $8.4 < \log M_{\text{BH}} < 8.9$ ; high  $M_{\text{BH}}$  with  $\log M_{\text{BH}} > 8.9$ , and three  $\lambda_{\text{Edd}}$  sub-samples: low  $\lambda_{\text{Edd}}$  sample with  $\log \lambda_{\text{Edd}} < -1.62$ ; medium  $\lambda_{\text{Edd}}$  with  $-1.62 < \log \lambda_{\text{Edd}} < -0.95$ ; high  $\lambda_{\text{Edd}}$  with  $\log \lambda_{\text{Edd}} > -0.95$ . Details of the  $M_{\text{BH}}$  and  $\lambda_{\text{Edd}}$  sub-samples can be found in Table 4.

### 5.2 Spectral stacking method

The rest-frame stacking method adopted in this work is similar to that presented in Corral et al. (2008, see also Falocco et al. 2012). Here we outline the main procedures of this method.

(i) Unfolding the spectrum: The intrinsic source spectra can be approximately reconstructed with the instrumental effects eliminated by unfolding the observed spectra. A model-dependent unfolding method is used to unfold the observed spectra. The `eufspec` command in XSPEC (Arnaud 1996) is applied to calculate the unfolded spectra, assuming a absorbed power-law with Galactic column density fixed at  $N_{\text{H}} = 2.0 \times 10^{20} \text{ cm}^{-2}$  given by Kalberla et al. (2005) in the XXL region and photon index obtained from the fitted value using the BXA method (see Section 4.1).

(ii) Rebin: We then correct the Galactic absorption and deredshift the unfolded spectra to the source rest-frame. The deredshifted rest-frame spectra have different energy bins, and thus



have to be rebinned into unified bins before stacking. To construct a new, unified bin scale, we group the rest-frame 2.1-10.1 keV energy range spectrum of each source with a bin width of 200 eV.

(iii) Stacking: We obtain the stacked spectrum by averaging the rebinned rest-frame unfolded spectra with simple arithmetic mean. We didn't rescale each spectrum by its flux due to the large uncertainty in choosing the proper rescaling factor for faint sources, which are the majority of our sample, as also pointed out in Iwasawa et al. (2012).

The PN and MOS spectra are stacked separately, to avoid any features induced by the stacking method and by the uncalibrated systematic differences between MOS and PN spectra.

### 5.3 Results

The rest-frame 2-10 keV stacked spectra of the sub-samples are shown in Figs. 13 (the redshift-luminosity sub-samples) and 14 (upper-panel: the  $\lambda_{\text{Edd}}$  sub-samples; lower-panel: the  $M_{\text{BH}}$  sub-samples). The PN and MOS stacked spectra are marked with blue and red points, respectively. In each plot, the ratio of the data to a best-fitting power-law continuum is also presented. There is evidence for excess emission at around 6.4 keV above the power-law continuum which could be attributed to the Fe neutral  $K\alpha$  emission line. In addition, potential highly ionized Fe K emission lines (e.g. the 6.67 keV Fe XXV and 6.97 keV Fe XXVI) are also detected in some of the stacked spectra, e.g. the LM sub-sample. No significant absorption feature is found in the stacked spectra of the sub-samples, which is consistent with the optical classification (the fraction of optical type-1 sources with  $N_{\text{H}} > 10^{21.5} \text{cm}^{-2}$  is quite low in each sub-sample, thus they will not dominate the stacked spectra).

Except for the Fe K emission lines, unidentified line features, especially with line energy peaked at the low energy band (e.g.  $< 5.5$  keV), are also shown in some of the stacked spectra. These line features can be due to systematic uncertainties of the data, as in most cases they are present only in one of the PN and MOS spectra. We carry out simulations to test whether these lines are artefacts and also to estimate the significance of the Fe K emission line. For each source in our sample, assuming a pure power-law model, we simulate 100 faked spectra using XSPEC. To match the observations, the exposure time, auxiliary and response matrix files for the sources in the sample are used in the simulations. For each sub-sample, we generate 100 stacked spectra by applying the same stacking method to the simulated source spectra. We further estimate the  $1\sigma$  and  $2\sigma$  confidence intervals by calculating the 3rd, 16th, 84th, 97th percentile values in each energy bin, which are shown as grey shadowed area in Fig 13 and 14. Contrary to what has been found in previous works (e.g. Corral et al. 2008), there are spurious lines features shown in the stacked spectra. This can be explained by the fact that our data on average have much lower S/N, thus larger systematic uncertainties, compared to the sample used in previous works. These lines, which are significantly detected in only one of the PN and MOS simulated stacked spectra, are not ubiquitously found in the stacked spectra. A spurious emission line feature at 6.4 keV ( $\sim 6.7$  keV or  $\sim 6.97$  keV), detected in both the PN and MOS stacked spectra, is found in about 6 (9) out of the 100 simulated spectra. The EWs of the spurious emission lines at 6.4 keV are around  $\sim 50 \pm 20$  eV.

The energy resolution of both EPIC PN and MOS cameras is  $\approx 0.15$  keV (FWHM) at 6.4 keV. A narrow line can be broadened by the stacking method described in Section 5.2, especially in the

unfolding procedure, due to instrumental effects. To examine this, we generate a series of spectra with high S/N using an intrinsically unresolved Gaussian line model (line width  $\sigma = 1$  eV). These simulated spectra have the same normalization, but different redshift,  $z = 0, 1, 2$ . We find that an intrinsically unresolved line manifests itself as a Gaussian profile in the unfolded spectrum. The line width increases with redshift and is in the range of 75 – 180 eV. These results are consistent with the conclusions reached by previous work (e.g. Corral et al. 2008; Iwasawa et al. 2012; Falocco et al. 2012; Liu et al. 2015).

We use XSPEC (version 12.8) to fit the stacked spectra. The FTOOLS task `flx2xsp` is used to convert the flux spectra into fits format which can be fitted using XSPEC. A base-line model consisting of a power-law and a Gaussian components, with all the parameters free, is used to jointly fit the PN and MOS stacked spectra. In some cases, the central energy of the Gaussian is fixed at 6.4 keV while the line width is fixed at 120 eV<sup>4</sup>, if these parameters cannot be well constrained due to the low S/N in the Fe line region of the stacked spectra.

#### 5.3.1 The redshift-luminosity sub-samples

A significant emission line feature peaking at 6.4 keV, which must be the neutral Fe  $K\alpha$  line, is detected ( $> 2\sigma$  level) in the stacked spectra of both the LL and LM sub-samples, as shown in the upper panel of Fig. 13, although it is only marginally detected at the  $2\sigma$  level in the MOS stacked spectrum of the LL sub-sample. The base-line model can fit the stacked spectra of the LL sub-sample well with the best-fitting photon index  $\Gamma = 1.85 \pm 0.03$ . The EW of the line is  $125 \pm 49$  eV, which is significantly higher than the EWs of the spurious 6.4 keV lines found in the simulations. In addition to the neutral Fe  $K\alpha$  line, an emission line feature peaked at around 7.0 keV is barely detected at  $2\sigma$  level in both the PN and MOS stacked spectra of the LM sub-sample. Thus a Gaussian component is added to the base-line model. The line width of the  $\sim 7.0$  keV emission line, which can not be well constrained, is fixed at 120 eV. We also fixed the line width of the 6.4 keV emission line at its best-fitting value, i.e.  $\sigma = 88$  eV. The best-fitting photon index is  $1.93 \pm 0.02$ . The line energy of the two Gaussian components are  $6.37 \pm 0.06$  and  $7.0 \pm 0.08$  keV (possibly corresponding to the highly ionized 6.97 keV Fe XXVI emission line), respectively. The neutral and highly ionized emission lines have comparable EWs, i.e.  $\text{EW}_{6.4\text{keV}} = 82 \pm 25$  and  $\text{EW}_{6.97\text{keV}} = 72 \pm 33$  eV.

The neutral Fe  $K\alpha$  line is only marginally detected at  $\sim 2\sigma$  level in the stacked spectra of the HM sub-sample (bottom-left panel of Fig. 13). A highly ionized Fe K emission line feature is present only in the MOS stacked spectrum of the HM sub-sample. It can be either due to the systematic uncertainty or a true high ionization emission line. In the first case, we fit the stacked spectra, excluding the 6.8 keV data point in the MOS spectrum, with the base-line model. The best-fitting slope of the power-law continuum is  $1.93 \pm 0.02$ . The line energy of the Gaussian component is  $6.43 \pm 0.10$  keV with the line width  $\sigma = 188_{-71}^{+104}$  eV. The EW of the

<sup>4</sup> As mentioned above, an unresolved narrow line will be broadened due to instrumental effects, and the artificial line broadening is redshift dependent, i.e. the line will be broader for high-redshift sources. We thus tried to fix the line width at different values (e.g. 100-150 eV). However, we did not find any significant difference. All calculated EWs of the emission line are consistent within their mutual uncertainties and will not affect our conclusion.

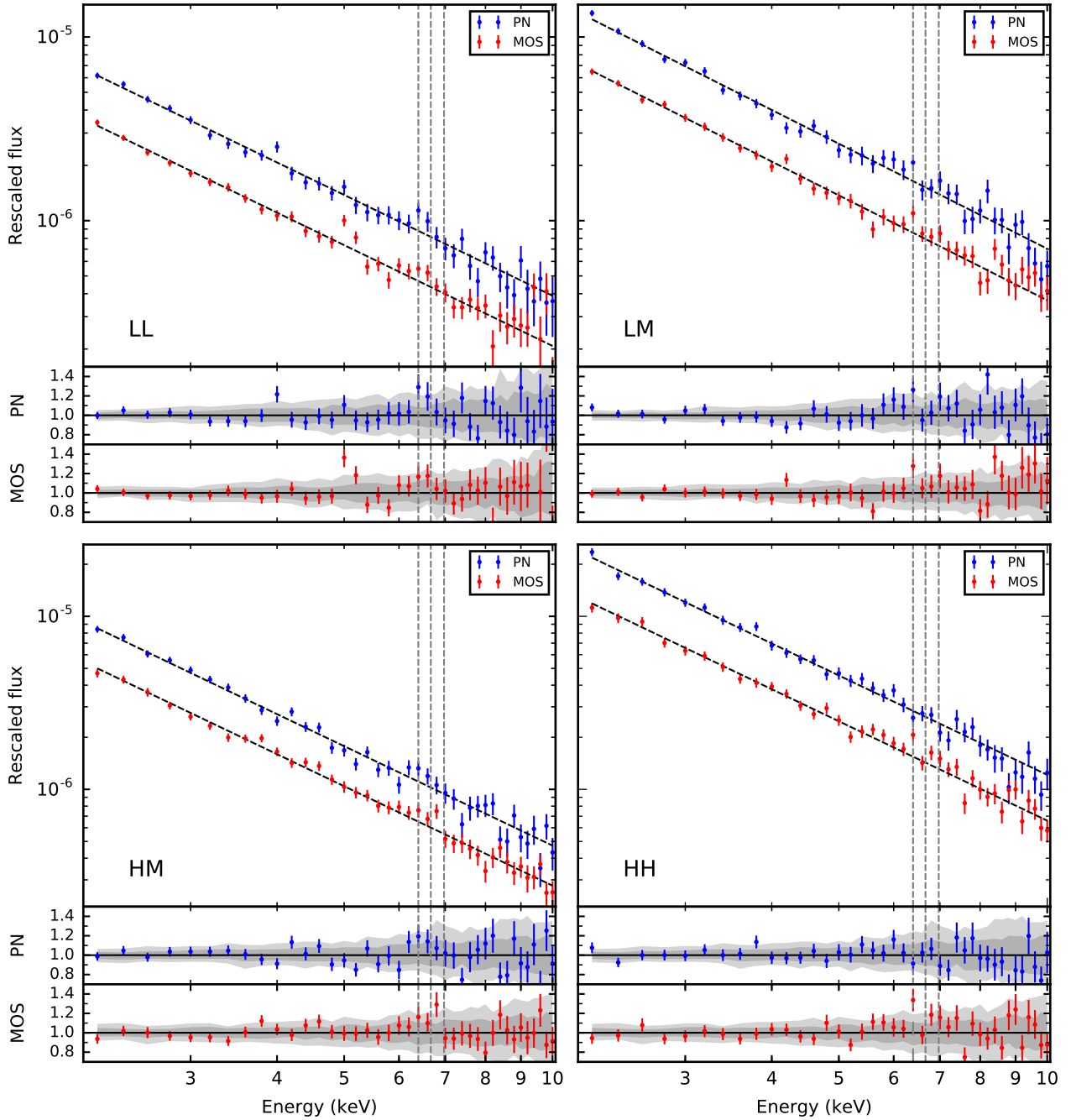


**Figure 13.** The stacked spectra of the PN (blue) and MOS (red) cameras for the redshift-luminosity sub-samples, with the best-fitting power-law continua (black dashed line) are shown in the *upper* plot of each panel (for sake of clarity, we rescaled the PN and MOS stacked spectra). The ratios of the stacked spectra to the best-fitting power-law continua are shown in the middle (PN) and bottom (MOS) plots of each panels. The  $1\sigma$  and  $2\sigma$  confidence intervals are marked as dark and light shaded areas, respectively. The grey dashed vertical lines are indications of the 6.4 keV, 6.67 keV and 6.97 keV emission lines. Details of each sub-sample can be found in Table 4

emission line is  $99 \pm 46$  eV. In the second case, the emission line detected in the PN spectrum should be a mixture of a neutral emission line with a high ionization emission line. We fit the PN and MOS spectra with the base-line plus a Gaussian component model. The line widths of the two Gaussian components are fixed at 120 eV. The best-fitting photon index is  $1.93 \pm 0.02$ . The line energies of the neutral and high ionization emission line are  $6.34 \pm 0.08$  and  $6.73 \pm 0.08$  keV, respectively. The equivalent width of the neutral

emission line is  $66 \pm 25$  eV while the highly ionized emission line has a line EW of  $69 \pm 34$  eV. The EW of the neutral emission line is consistent with the first case.

No significant line features are detected in the PN stacked spectrum of the HH sub-sample (bottom-right panel of Fig. 13), while an emission line peaking at  $\sim 6.4$  keV and a possible highly ionized emission line are present in the MOS stacked spectrum. We fixed the line energy of the Gaussian component at 6.4 keV and the

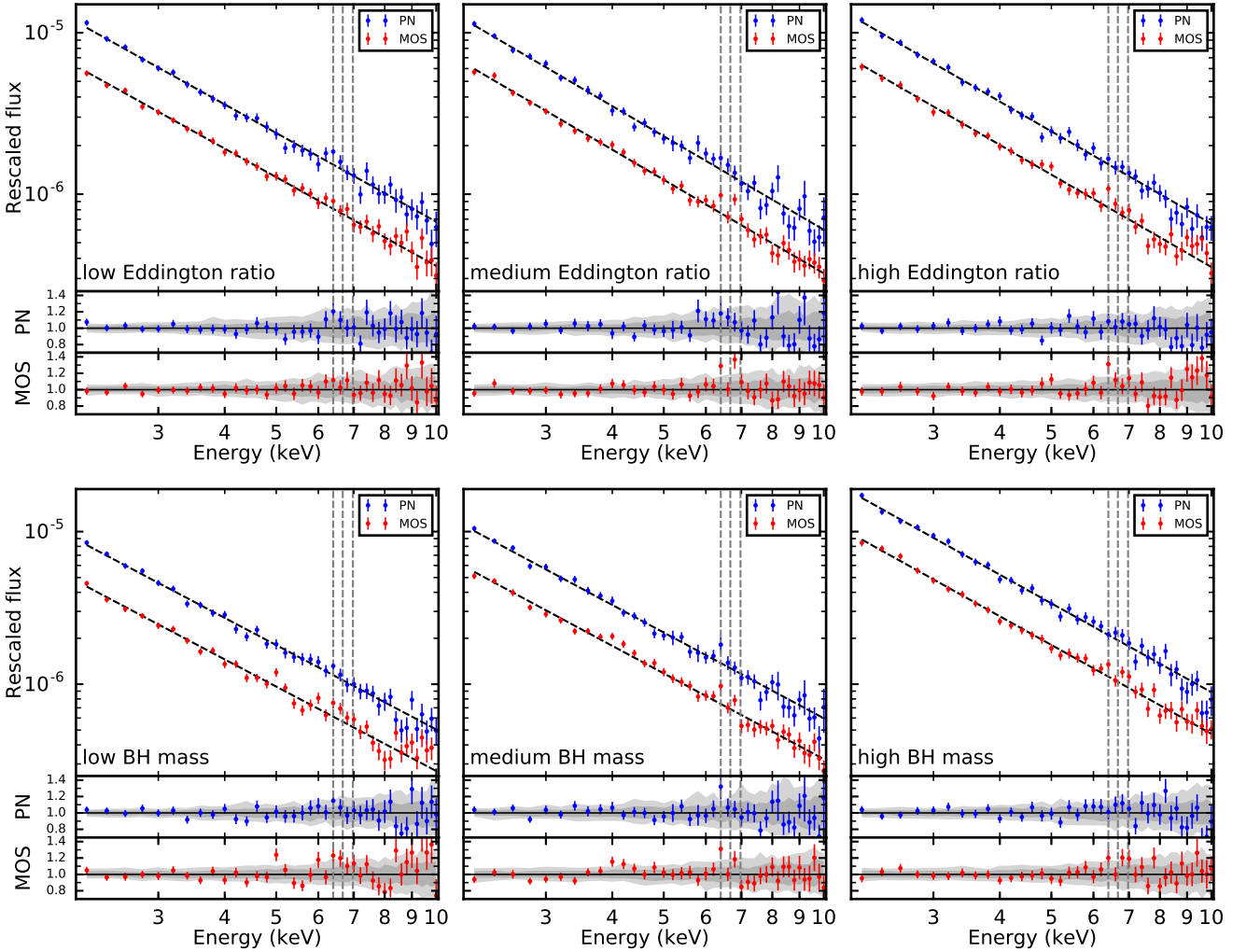


**Figure 14.** Same as Fig. 13, but for  $\lambda_{\text{Edd}}$  (upper panel) and  $M_{\text{BH}}$  (lower panel) sub-samples. Details of each sub-sample can be found in Table 4

line width at 120 eV. The best-fitting photon index is  $1.92 \pm 0.02$  and the EW of the emission line is less than 60 eV. We also try to only fit the MOS spectrum with the base-line model plus a Gaussian component. The line energy of the first emission line, which is consistent with a neutral Fe  $K\alpha$  line as shown in the bottom-right panel of Fig. 13, is fixed at 6.4 keV. The best-fitting photon index is  $1.89 \pm 0.03$ . The line width of the 6.4 keV line is found to be  $\lesssim 100$  eV. The EW of the neutral Fe  $K\alpha$  line is  $68 \pm 40$  eV. The line energy of the second Gaussian component is  $6.90 \pm 0.10$  keV (to estimate the uncertainty, the line widths of the two Gaussian components are fixed to their best-fitting values) with EW of  $80 \pm 44$  eV. The line width of this emission line is found to be 121 eV with an upper limit of 303 eV.

### 5.3.2 The Eddington ratio sub-samples

As shown in Fig. 14, an emission line feature peaking at around 6.4 keV is marginally seen in the stacked PN spectrum ( $\sim 2\sigma$  level) of the low  $\lambda_{\text{Edd}}$  sub-sample, while it is only tentatively detected in the MOS stacked spectrum ( $\approx 1\sigma$  level). The best-fitting photon index of the power-law continuum in the base-line model is  $1.84 \pm$

$0.02$ . The EW of the Gaussian component, with  $E = 6.38^{+0.10}_{-0.08}$  keV and  $\sigma = 150^{+104}_{-150}$  eV, is  $73 \pm 30$  eV.

Two emission line features are detected at  $2\sigma$  level in the MOS stacked spectrum of the medium  $\lambda_{\text{Edd}}$  sub-sample, while only a broad line feature (e.g.  $\sigma \sim 400$  eV) is found in the PN stacked spectrum. We first jointly fit the stacked spectra with the base-line model plus a Gaussian component. The line energy of the highly ionized emission line is fixed at its best-fitting value,  $E = 6.86$  keV. The best-fitting photon index of the power-law component in the base-line model is  $\Gamma = 1.95 \pm 0.02$ . The line energy of the neutral emission line is  $6.38 \pm 0.24$  keV with the line width  $\sigma = 120^{+260}_{-50}$  eV. The EW of the neutral emission line is  $88 \pm 30$  eV. The EW of the high ionization emission line is  $56 \pm 21$  eV, with an upper limit of the line width  $\sigma = 101$  eV. We also fit the stacked spectra with only the base-line model, excluding the energy range around  $\sim 6.8$  keV in the MOS stacked spectrum. In this case, the best-fitting slope of the continuum as well as the parameters of the Gaussian component in the base-line model are in good agreement with the results from the base-line model plus a Gaussian component.

Although an emission line at 6.4 keV is not significantly detected in the PN stacked spectrum of the high  $\lambda_{\text{Edd}}$  sub-sample,

**Table 5.** Estimated parameters for each sub-sample

Samples	JOINT				EPIC PN				EPIC MOS			
	$\Gamma^a$	$E_{\text{Gau}}(\text{keV})$	$\sigma(\text{eV})$	EW(eV)	$\Gamma^b$	$E_{\text{Gau}}(\text{keV})$	$\sigma(\text{eV})$	EW(eV)	$\Gamma^b$	$E_{\text{Gau}}(\text{keV})$	$\sigma(\text{eV})$	EW(eV)
LOW LOW	1.85	$6.46 \pm 0.08$	$190^{+91}_{-86}$	$125 \pm 49$	1.87	$6.46 \pm 0.08$	$149^{+129}_{-147}$	$139 \pm 64$	1.83	$6.46 \pm 0.13$	$216^{+119}_{-203}$	$110 \pm 67$
LOW MED	1.93	$6.37 \pm 0.06$	$88^{+65}_{-86}$	$82 \pm 25$	1.97	$6.33 \pm 0.08$	$120^f$	$111 \pm 48$	1.89	$6.40 \pm 0.07$	$83^{+83}_{-83}$	$73 \pm 42$
HIG MED*	1.93	$6.43 \pm 0.10$	$188^{+104}_{-71}$	$99 \pm 46$	1.97	$6.48 \pm 0.13$	$199^{+128}_{-78}$	$136 \pm 72$	1.89	$6.43 \pm 0.14$	$120^f$	$59 \pm 32$
HIG HIG	1.91	$6.40^f$	$120^f$	$< 60$	1.95	$6.40^f$	$120^f$	$< 30$	1.89	$6.40^f$	$< 100$	$68 \pm 40$
LOW EDD	1.84	$6.38 \pm 0.10$	$150^{+103}_{-142}$	$73 \pm 30$	1.89	$6.41 \pm 0.09$	$160^{+93}_{-65}$	$111 \pm 50$	1.80	$6.40^f$	$120^f$	$< 70$
MED EDD*	1.95	$6.38 \pm 0.24$	$120^{+260}_{-50}$	$88 \pm 30$	1.97	$6.42 \pm 0.14$	$120^f$	$98 \pm 46$	1.92	$6.37 \pm 0.08$	$63^{+61}_{-63}$	$70 \pm 59$
HIG EDD	1.91	$6.46 \pm 0.06$	$120^f$	$60 \pm 26$	1.94	$6.40^f$	$120^f$	$< 56$	1.87	$6.40^f$	$71^{+52}_{-71}$	$71 \pm 32$
LOW MBH	1.86	$6.48 \pm 0.14$	$< 470$	$73 \pm 30$	1.88	$6.43 \pm 0.20$	$123^{+77}_{-123}$	$63 \pm 40$	1.83	$6.46 \pm 0.09$	$120^f$	$67 \pm 47$
MED MBH*	1.88	$6.40^f$	$< 104$	$72 \pm 30$	1.93	$6.40 \pm 0.07$	$108^{+127}_{-96}$	$113 \pm 47$	1.84	$6.40^f$	$69^{+46}_{-69}$	$71 \pm 31$
HIG MBH	1.96	$6.32 \pm 0.11$	$119^{+69}_{-54}$	$45 \pm 20$	1.96	$6.40^f$	$120^f$	$< 54$	1.94	$6.36 \pm 0.07$	$120^f$	$64 \pm 32$

\*: Only the results fitted with the base-line plus a Gaussian component model are shown here.

*a*: The typical  $1\sigma$  uncertainty is 0.02.

*b*: The typical  $1\sigma$  uncertainty is 0.03.

*f*: The line width of the Gaussian component is fixed.

there is evidence for such an emission feature in the MOS stacked spectrum ( $> 2\sigma$  level). We fixed the line width at 120 eV. The best-fitting photon index is  $1.91 \pm 0.02$  if the stacked spectra are fit with the base-line model. The line energy is  $E = 6.46 \pm 0.06$ , consistent with the neutral Fe K $\alpha$  line. The EW of the line is  $60 \pm 26$  eV.

### 5.3.3 The BH mass sub-samples

The stacked spectra of the low  $M_{\text{BH}}$  sub-sample are fitted with the base-line model. The best-fitting photon index of the continuum is  $1.86 \pm 0.03$ . The line energy of the Fe K line, which is detected barely at  $\sim 2\sigma$  level, is  $6.48 \pm 0.14$  keV with line width  $\sigma = 99$  eV (with an upper limit of  $\sim 470$  eV). The EW of the line is  $73 \pm 30$  eV.

An emission peaked at  $\sim 6.4$  keV is significantly detected ( $> 2\sigma$  level) in both the PN and MOS stacked spectra of the medium  $M_{\text{BH}}$  sub-sample. A line feature with energy at  $\sim 6.7$  keV is also presented in the MOS stacked spectrum. We first fit the stacked spectra with the base-line model, excluding the line feature shown in the MOS stacked spectrum. The slope of the power-law continuum is  $1.88 \pm 0.02$ . The line energy of the Gaussian component is consistent with the neutral Fe K $\alpha$  line,  $E = 6.38 \pm 0.04$  keV. The best-fitting line width is 86 eV, with an upper limit of 121 eV. The EW of the neutral line is  $89 \pm 28$  eV. We also fit the stacked spectra with the base-line model plus a Gaussian component. The line energy of the two Gaussian components are fixed at 6.4 and 6.7 keV, respectively. The line width of the neutral emission line is left to be free, while it is fixed at 120 eV for the 6.7 keV emission line. The fitting results are consistent with the results in the first case, i.e.  $\Gamma = 1.88 \pm 0.02$ ,  $\sigma < 104$  eV and  $\text{EW} = 72 \pm 30$  eV. The EW of the high ionized emission line is 24 eV with an upper limit of 50 eV.

A potential highly ionized emission line is shown in both the PN and MOS stacked spectra of the high  $M_{\text{BH}}$  sub-sample, while a neutral Fe K emission line is only presented in the MOS stacked spectrum ( $\sim 2\sigma$  level). We fit the stacked spectra with the base-line model plus a Gaussian component. The line width of the neutral Fe K emission line is fixed at 120 eV while the line energy of the highly ionized emission line is fixed at its best-fitting value

$E = 6.85$  keV. The best-fitting photon index is  $1.96 \pm 0.02$ . The line energy of the neutral emission line is  $6.32 \pm 0.11$  keV. The line width of the high emission line can be well constrained, i.e.  $\sigma = 119^{+69}_{-54}$  eV. The EWs of the neutral and ionized emission line are  $45 \pm 20$  and  $64 \pm 30$  eV, respectively.

The results of the spectral fitting can be found in Table 5. We also fit the PN and MOS spectra of each sub-sample separately in order to check the consistency between the PN and MOS stacked spectra. The results are also included in Table 5. In each sub-sample, the line EWs estimated from the PN and MOS spectra are in good agreement with each other while the photon indices are consistent within 90 per cent confidence level (the typical 90 per cent confidence level of  $\Gamma$  is 0.06).

## 6 DISCUSSION

### 6.1 On the X-ray Baldwin effect in type-1 AGN

The left panel of Fig. 15 shows the EWs of the Fe K $\alpha$  line against the median  $2 - 10$  keV X-ray luminosity in the redshift-luminosity sub-samples. The EWs of the Fe K $\alpha$  line as well as the  $1\sigma$  uncertainties are calculated from the spectral modelling as described in Section 4.1. The anti-correlation found in previous work,  $\log \text{EW}_{6.4\text{keV}} = (1.73 \pm 0.03) + (-0.17 \pm 0.03) \log L_{2-10\text{keV},44}$  (Bianchi et al. 2007), as well as its  $1\sigma$  uncertainty are also shown as solid and dashed grey lines, respectively. The two values of the EWs for the HM sub-sample, which are shown as red and green points, are calculated assuming different models (see Section 5.3 above). It shows a trend that the EW of the narrow Fe K $\alpha$  line decreases with the X-ray luminosity, i.e. the so-called X-ray Baldwin effect. The anti-correlation was first found by Iwasawa & Taniguchi (1993) and confirmed by subsequent studies (e.g. Nandra et al. 1997; Page et al. 2004; Jiang, Wang, & Wang 2006; Bianchi et al. 2007; Shu, Yaqoob, & Wang 2010; Chaudhary et al. 2010; Shu, Yaqoob, & Wang 2011; Falocco et al. 2013; Ricci et al. 2014). However, using a sample of quasars selected from the Palomar-Green (PG) Bright Quasar Survey, Jiménez-Bailón et al. (2005) questioned the significance of the effect. They found



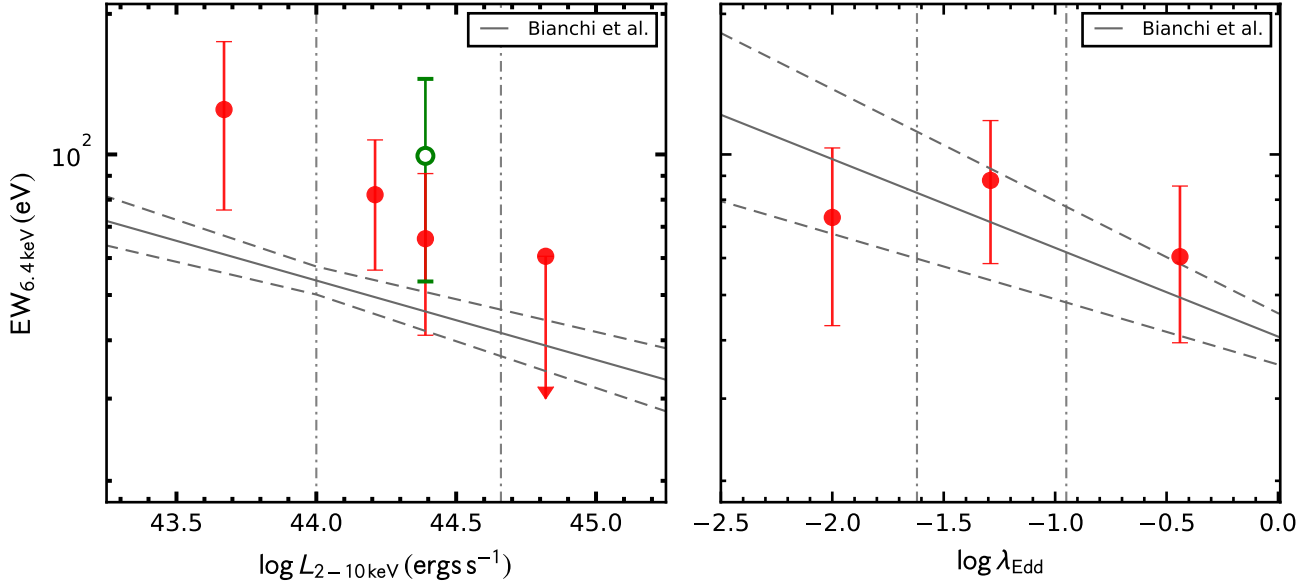


**Figure 15.** Left: the X-ray luminosity versus EWs of Fe K $\alpha$  line in the redshift-luminosity sub-samples. The green point shows the EWs of the Fe K $\alpha$  line estimated with the base-line only (excluding the high ionization line feature) for the HM sub-sample. Right: the  $\lambda_{\text{Edd}}$  versus EWs of Fe K $\alpha$  line in the  $\lambda_{\text{Edd}}$  sub-samples. The relations presented in Bianchi et al. (2007) as well as the  $1\sigma$  uncertainties are also shown with solid and dashed lines, respectively. The vertical dash-dotted lines indicate the luminosity boundaries for the sub-samples.

that the EW of the Fe K $\alpha$  line is more likely to be constant for  $L_{2-10\text{keV}} \lesssim 10^{45} \text{ erg s}^{-1}$  and a step-wise decrease above this threshold, though they could not rule out a smooth power-law dependence. Krumpal et al. (2010) argued that the EWs of the Fe K $\alpha$  line in their sample (three sources with  $L_{2-10\text{keV}} > 4 \times 10^{44} \text{ erg s}^{-1}$ ) were systematically higher than the expected value from the X-ray Baldwin effect (see also Chaudhary et al. 2010). On the contrary, our results suggest that the average EWs of the medium (i.e.  $44.00 < \log L_{2-10\text{keV}} < 44.66$ ) and high luminosity (i.e.  $44.66 < \log L_{2-10\text{keV}} < 45.60$ ) bins are still consistent with the X-ray Baldwin relation found in previous studies (e.g. Bianchi et al. 2007). We caution that, as remarked by Jiménez-Bailón et al. (2005) and Jiang, Wang, & Wang (2006), these differences may be potentially due to the contribution from radio-loud sources, which generally show weak Fe K $\alpha$  emission line (Reeves & Turner 2000). However, they are unlikely to dominate the stacked spectra considering that only  $\sim 15$  per cent of AGN are radio-loud (Urry & Padovani 1995).

The origin of the X-ray Baldwin effect, which may provide important insights into the physics of AGN emission, is still unclear. One possible explanation is the decrease of the covering factor of the torus with X-ray luminosity (e.g. Page et al. 2004; Zhou & Wang 2005). Ricci et al. (2013a) showed that the observed X-ray Baldwin effect and its slope can be produced with this explanation. To provide an independent test of this scenario, Fig. 16 (left and middle panels) shows the reflection fraction distribution of the low/high-luminosity and low/high-redshift sub-samples. We also plot the reflection fraction distribution of the three  $\lambda_{\text{Edd}}$  sub-samples in the right panel of Fig. 16. There is an indication that the low-luminosity sub-sample has statistically higher reflection fraction than the high-luminosity sub-sample. A Kolmogorov-Smirnov (K-S) test shows a significant difference between these two sub-samples ( $P_{\text{KS}} = 1.0 \times 10^{-17}$ ), while the probability that the low/high medium sub-samples are drawn from the same par-

ent distribution is 60 per cent. The reflection distributions of the medium and the high  $\lambda_{\text{Edd}}$  sub-samples are different from the low  $\lambda_{\text{Edd}}$  sub-sample ( $P_{\text{KS}} < 3 \times 10^{-4}$ ), while no significant difference is found between these two sub-samples ( $P_{\text{KS}} = 0.77$ ). These results, which are consistent with the results obtained from the spectral stacking, may suggest that the X-ray Baldwin effect is more related to the X-ray luminosity and unlikely to be due to the  $\lambda_{\text{Edd}} - \Gamma$  relation (e.g. Ricci et al. 2013b, see right panel of Fig. 15). Our results also indicate that the structure of the dusty torus in type-1 AGN does not evolve strongly with redshift. The difference of the reflection fraction distribution in the low and high luminosity sub-samples supports the luminosity-dependent covering factor scenario, i.e. the covering factor of the torus decrease with the X-ray luminosity.

The X-ray Baldwin effect can also be explained by a luminosity-dependent ionization state of the emitting material (Nandra et al. 1997; Nayakshin 2000) or by AGN variability (Jiang, Wang, & Wang 2006; Shu et al. 2012). In the first case, we may expect the change of ionization state of the Fe line in different sub-samples. However, a highly ionized Fe K line (Fe XXVI) is unambiguously detected only in the LM sub-sample. No clear trend of the change of ionization state with X-ray luminosity is found in our results. Our analysis does not support the luminosity-dependent ionization state scenario. Regarding variability as a possible origin, with a large number of AGN in our sample, which should include sources in different luminosity states in each sub-sample, we should expect a nearly constant Fe K $\alpha$  EW in different sub-samples, if the X-ray Baldwin effect can be purely explained by AGN variability. Our results seem to disfavour this interpretation.

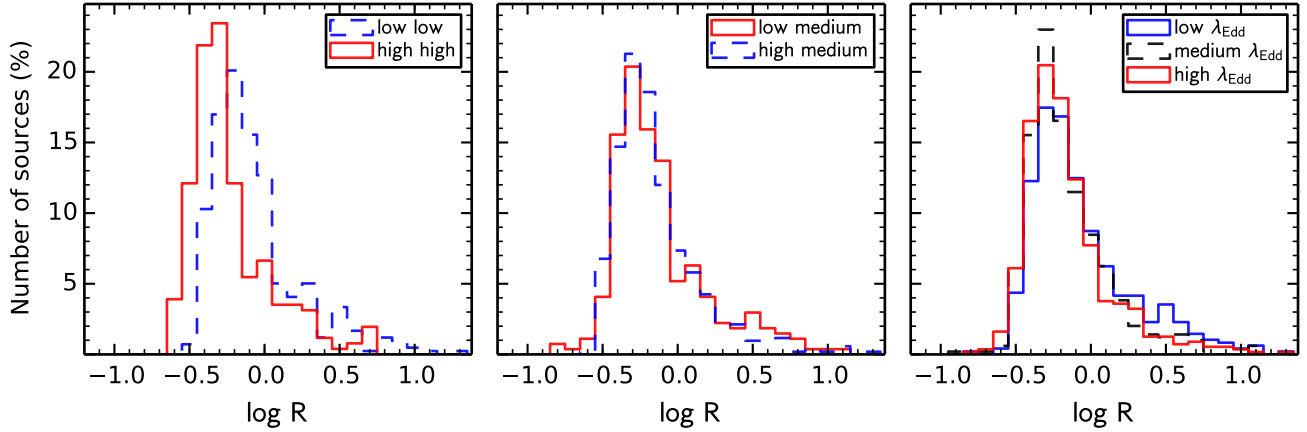


**Figure 16.** The distributions of the relative reflection normalization for the different sub-samples. The reflection normalization, which is equal to the reflection fraction, is estimated with the BXA method.

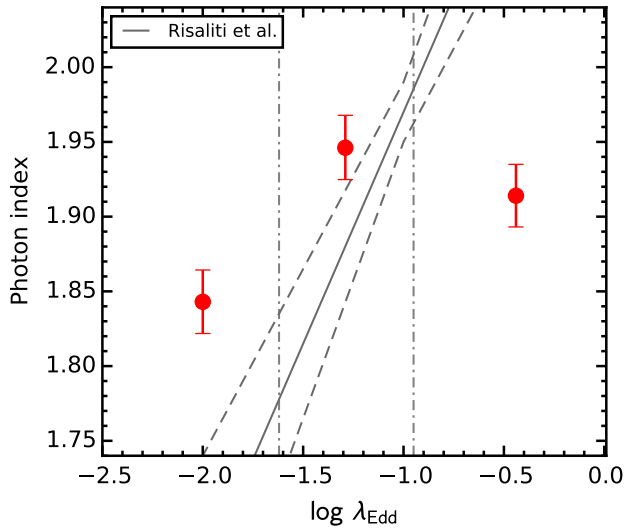


**Figure 17.** Photon index vs.  $\lambda_{\text{Edd}}$  for three  $\lambda_{\text{Edd}}$  subsamples. The solid and dashed lines show the relation as well as the  $1\sigma$  uncertainties in Risaliti, Young, & Elvis (2009), respectively. The vertical dash-dotted lines indicate the  $\lambda_{\text{Edd}}$  boundaries for the three sub-samples.

## 6.2 On the correlation between the photon index and Eddington ratio

A significant positive correlation between the photon index  $\Gamma$  and  $\lambda_{\text{Edd}}$  has been found in many previous studies (e.g. Lu & Yu 1999; Wang, Watarai, & Mineshige 2004; Shemmer et al. 2006, 2008; Risaliti, Young, & Elvis 2009; Brightman et al. 2013). In Fig. 17 we show the best-fitting  $\Gamma$  against the median values of  $\lambda_{\text{Edd}}$  for the Eddington ratio sub-samples. The solid and dashed lines show the relation as well as the  $1\sigma$  uncertainties found in Risaliti, Young, & Elvis (2009), respectively. Unlike the strong correlation presented in the studies mentioned above, our results suggest that the  $\Gamma$  stays constant or decreases with  $\lambda_{\text{Edd}}$  if  $\lambda_{\text{Edd}}$  is high, e.g.  $\lambda_{\text{Edd}} > 0.1$ . Ai et al. (2011) suggested that the  $\Gamma$  of the sources in their sample, which are narrow-line Seyfert 1 galaxies (NLS1s) with high ac-

cretion rate, are systematically below the Risaliti, Young, & Elvis (2009) relation. This flattening of the  $\Gamma - \lambda_{\text{Edd}}$  relation was also confirmed by Kamizasa, Terashima, & Awaki (2012) with a sample which have small  $M_{\text{BH}}$  and high  $\lambda_{\text{Edd}}$ . Our result, which also shows a flattening of the relation, is consistent with these studies.

Gu & Cao (2009, see also Constantin et al. 2009; Younes et al. 2011) found an anti-correlation between the  $\Gamma$  and  $\lambda_{\text{Edd}}$  in a sample of low-luminosity AGN (LLAGN), which typically have low  $\lambda_{\text{Edd}}$  (i.e.  $\lambda_{\text{Edd}} < 10^{-3} - 10^{-2}$ ). Based on this anti-correlation they proposed that the X-ray emission of LLAGN could originate from the Comptonization process in advection-dominated accretion flow (ADAF), in which case the flattening of  $\Gamma$  is due to the increase of the Compton- $y$  parameter with Eddington ratio. The positive correlation, generally shown in sources with  $\lambda_{\text{Edd}} > 10^{-3} - 10^{-2}$  (Younes et al. 2011), could be explained by a disc-corona system. In this case, the 2–10keV X-ray emission is generally thought to be due to the Compton up-scattering of seed soft photons from a standard optically thick geometrically thin accretion disc (Shakura & Sunyaev 1973) in a hot corona (Haardt & Maraschi 1991, 1993). The steepening of  $\Gamma$  can be interpreted as enhanced emission from the accretion disc more effectively cooling the corona as  $\lambda_{\text{Edd}}$  increases (Pounds, Done, & Osborne 1995; Haardt & Maraschi 1991, 1993; Wang, Watarai, & Mineshige 2004). If the standard accretion disc model and the disc-corona system is still appropriate in the high  $\lambda_{\text{Edd}}$  regime, the flattening of the  $\Gamma - \lambda_{\text{Edd}}$  relation, as presented in our result (see also Ai et al. 2011; Kamizasa, Terashima, & Awaki 2012), suggest that the inverse Compton scattering is saturated in sources with high  $\lambda_{\text{Edd}}$ . On the other hand, the structure of the accretion disc may change if the  $\lambda_{\text{Edd}}$  is high, i.e. a slim disc (Abramowicz et al. 1988) instead of the standard thin disc. If this is the case, the flattening of the relation can also be explained under the assumption that the temperature of the slim disc does not change anymore when  $\lambda_{\text{Edd}}$  exceeds a certain value. Thus increasing the  $\lambda_{\text{Edd}}$  will not produce more soft X-ray photons, leading to a flatter  $\Gamma - \lambda_{\text{Edd}}$  relation. We caution here that the uncertainties in the  $M_{\text{BH}}$  measurements, which may suffer from many systematic effects such as orientation (Shen 2013; Shen & Ho 2014), can potentially destroy the  $\Gamma - \lambda_{\text{Edd}}$  correlation, especially in the high  $\lambda_{\text{Edd}}$  sub-sample which consist of a large fraction of sources using the less reliable CIV and Mg II based virial BH masses.

As mentioned in Iwasawa et al. (2012), the flattening of the  $\Gamma$  in the high  $\lambda_{\text{Edd}}$  stacked spectrum may potentially be due to absorption. This is unlikely the case in our sample as no significant difference of the column density distribution of the three  $\lambda_{\text{Edd}}$  sub-samples is found.

### 6.3 Non-detection of the broad line in the BH mass sub-samples?

A broad line profile was seen in the previous X-ray spectral stacking studies of AGN (e.g. Streblyanska et al. 2005; Corral et al. 2008; Iwasawa et al. 2012; Falocco et al. 2014; Liu et al. 2015), although typically with low significance. The broad Fe  $K\alpha$  line, which is generally thought to be broadened due to the strong gravitational field of the central SMBH, can be used to constrain the spin of BH (Brenneman & Reynolds 2006; Dauser et al. 2010). The SMBH growth is mainly due to accretion of matter during active phases over cosmological times. For a standard optical thick geometry thin accretion disc, the radiation efficiency depends solely on the spin of BH. Thus we may expect a dependence of the  $M_{\text{BH}}$  growth rate on the spin of the BH. Volonteri et al. (2013) showed that spin as a function of  $M_{\text{BH}}$  in galaxies under different accretion scenarios (i.e. coherent or chaotic accretion) are different. In principle, by comparing the line profile detected in the stacked spectra of different  $M_{\text{BH}}$  samples may help us understand the accretion history of the BH. However, as shown in Fig. 14, no apparent broad line features are detected in the three  $M_{\text{BH}}$  sub-samples. This should not be a surprise since the S/N of the stacked spectra is still too low to detect the broad line (e.g. total photon counts  $> 1.5 \times 10^5$  is required to detect the broad line, de La Calle Pérez et al. 2010). A large sample of AGN with well measured  $M_{\text{BH}}$  from optical spectra (e.g. SDSS IV/SPIDERS) will be helpful to understand the relation between BH spin and  $M_{\text{BH}}$ .

### 6.4 On the inconsistency between X-ray/optical classifications

As shown in Fig. 9, the  $N_{\text{H}}$  distribution of type-1 AGN is peaked at values (e.g.  $\sim 20.7$ ) consistent with little or no X-ray absorption while most of the type-2 AGN have  $N_{\text{H}}$  larger than  $10^{21} \text{ cm}^{-2}$ . However, about  $\sim 40$  per cent of both type-1 and type-2 AGN show discrepancies between their optical classifications and the absorption column densities obtained from the X-ray spectral fitting, i.e. optical type-1 AGN with indications of high X-ray absorption or type-2 AGN with X-ray spectra showing no significant absorption.

Following Merloni et al. (2014), sources with  $N_{\text{H}} > 10^{21.5} \text{ cm}^{-2}$  are considered to be X-ray obscured. We define type-11 AGN as those which are optically classified as type-1 AGN with unobscured X-ray spectra; type-22 AGN are instead optical type-2 objects which are also obscured at X-ray. Type-12 AGN are type-1 objects which are X-ray obscured; conversely we call type-21 as optical type-2 AGN which have X-ray spectra consistent with no obscuration. Each of these types are divided into different bins on the basis of the redshift and X-ray luminosity. The high-redshift high-luminosity type-11/12 (hhtype-11/12) bin include all the type-11/12 sources with  $z > 1.36$  and  $\log L_{2-10\text{keV}} > 44 \text{ erg s}^{-1}$ . The low-redshift ( $z < 1.36$ ) type-11/12 sources are divided into two luminosity bins, i.e. low-luminosity bin with  $\log L_{2-10\text{keV}}$  in the range  $42 - 44 \text{ erg s}^{-1}$  (ltype-11/12) and high luminosity bin with  $\log L_{2-10\text{keV}}$  larger than  $44 \text{ erg s}^{-1}$  (htype-11/12). The same procedure is applied to the low-redshift

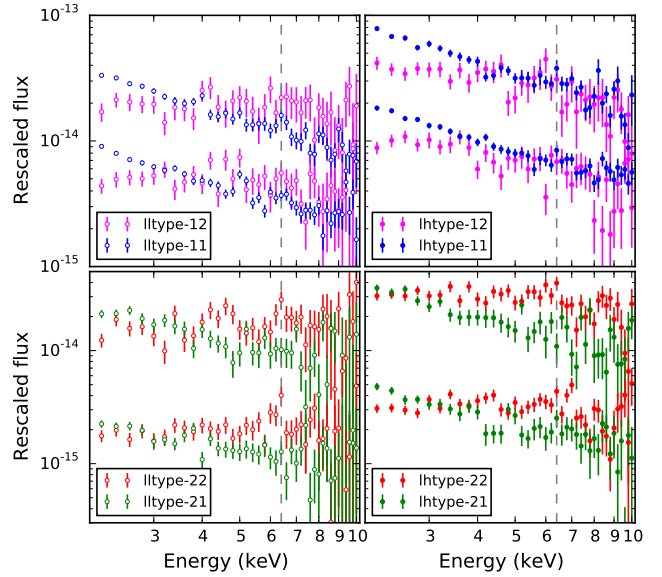


**Figure 18.** Upper-left panel: the stacked spectra of the PN (with higher rescaled flux) and MOS (with lower rescaled flux) spectra for the low-luminosity low-redshift optical classified type-1 AGN with (open magenta, *ltype-12*) and without (open blue, *ltype-11*) X-ray absorption signature. Upper-right panel: the same as the upper-left panel but with high-luminosity ones (filled magenta, *lhtype-12*; filled blue, *lhtype-11*). Bottom-left panel: same as above but for the low-luminosity low-redshift optical classified type-2 AGN with (open red, *ltype-22*) and without (open green, *ltype-21*) X-ray absorption signature. Bottom-right panel: the same as the bottom-left panel but with high-luminosity ones (filled red, *lhtype-22*; filled green, *lhtype-21*). The grey dashed vertical line indicates the 6.4 keV emission line.

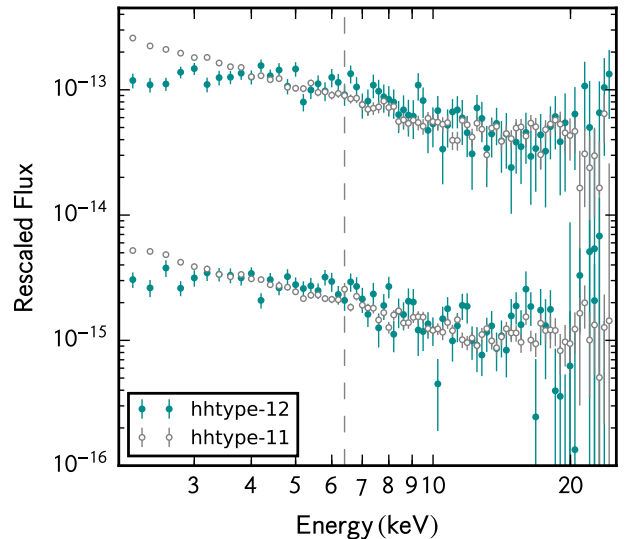


**Figure 19.** The 2-25 keV PN (with higher rescaled flux) and MOS (with lower rescaled flux) stacked spectra for the high-redshift high-luminosity type-11 (hhtype-11, grey points) and type-12 (hhtype-12, cyan points). The grey dashed vertical line indicates the 6.4 keV emission line.

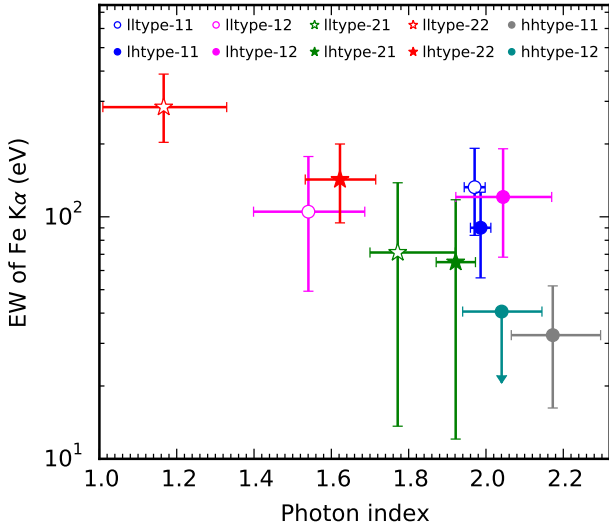


**Figure 20.** The equivalent width of the Fe  $K\alpha$  line versus the photon index. The optical type-1 AGN are shown with empty/filled circles while type-2 are shown with empty/filled stars.

( $z < 1.36$ ) type-21/22 sources but with different luminosity range, i.e. lltype-21/22 with  $\log L_{2-10\text{keV}}$  in the range 42 – 43  $\text{erg s}^{-1}$  and lhtype-21/22 with  $\log L_{2-10\text{keV}}$  in the range 43 – 44  $\text{erg s}^{-1}$ .

To investigate the properties of these different types, the same X-ray spectral stacking method described in Section 5.2 is applied to each bin. In Fig. 18, we show the stacked spectra of all the low redshift bins. The stacked spectra of the hhtype-11/12 are plotted in Fig 19. We fit the stacked spectra with a model including a photoionization absorption component, a power-law continuum, and, if necessary, a Gaussian component (PHABS\*[PO+GAUSSIAN]). Some of the best-fitting parameters as well as the EWs of the Gaussian component are listed in Table 6. The measured column densities of the stacked spectra are well in agreement with the values of individual source in each bin, i.e. bins with  $N_{\text{H}}$  higher/less than  $10^{21.5} \text{ cm}^{-2}$  show X-ray absorption larger/smaller than  $\sim 10^{22} \text{ cm}^{-2}$ . This implies that the column density of an individual source obtained through the spectral modelling method, though with large uncertainties due to the low S/N, are statistically reliable.

#### 6.4.1 X-ray obscured type-1 AGN

The *upper-left* panel of Fig. 18 shows the stacked spectra of both the X-ray unobscured (*open blue* points) and obscured (*open magenta* points) low-redshift low-luminosity optical type-1 AGN (lltype-11/12). The *upper-right* panel of Fig. 18 shows the same plot but for the high-luminosity ones (lhtype-11/12). As clearly demonstrated in the plots, both the lltype-11 and lhtype-11 AGN exhibit a featureless power-law with similar photon index (see upper panel of Fig. 18, with open blue for lltype-11 and filled blue for lhtype-11). The EW of the Fe line seems to be weaker (though with large errors, see Table 6) in the lhtype-11 AGN, which is consistent with the X-ray Baldwin effect and the results presented in Section 6.1. The stacked spectra of the lltype-12 and lhtype-12 AGN are quite different, except that both show significant obscuration in their stacked X-ray spectra. The photon index of the lhtype-12 bin is  $\Gamma = 2.04 \pm 0.13$  which is consistent with the typical value found in type-1 AGN. In contrast, the lltype-12 AGN has a signifi-

**Table 6.** Estimated parameters for the  $N_{\text{H}}$  samples

samples	$\Gamma$	$N_{\text{H}} (10^{22} \text{ cm}^{-2})$	$EW_{6.4 \text{ keV}} (\text{eV})$	#src
lltype-11	$1.97 \pm 0.03$	$< 0.08$	$133^{+59}_{-49}$	363
lhtype-11	$1.99 \pm 0.03$	$< 0.06$	$90 \pm 36$	251
hhtype-11	$2.17 \pm 0.13$	$0.20 \pm 0.16$	$32^{+20}_{-16}$	662
lltype-12	$1.54 \pm 0.14$	$1.56 \pm 0.60$	$105^{+72}_{-56}$	55
lhtype-12	$2.04 \pm 0.13$	$1.66 \pm 0.49$	$121^{+70}_{-53}$	38
hhtype-12	$2.04 \pm 0.10$	$2.97 \pm 0.39$	$< 40.6$	111
lltype-22	$1.17 \pm 0.16$	$0.93 \pm 0.59$	$284^{+105}_{-81}$	66
lhtype-22	$1.62 \pm 0.09$	$1.83 \pm 0.38$	$143^{+57}_{-49}$	118
lltype-21	$1.77^{+0.15}_{-0.07}$	$< 0.52$	$71^{+67}_{-57}$	127
lhtype-21	$1.92 \pm 0.05$	$< 0.30$	$65^{+73}_{-53}$	134

lltype-11/lhtype-11: low-redshift low/high-luminosity X-ray unobscured optical type-1 AGN; hhtype-11: high-redshift high-luminosity X-ray unobscured optical type-1 AGN; lltype-12/lhtype-12: low-redshift low/high-luminosity X-ray obscured optical type-1 AGN; hhtype-12: high-redshift high-luminosity X-ray obscured optical type-1 AGN; lltype-21/lhtype-21: low-redshift low/high-luminosity X-ray unobscured optical type-2 AGN; lltype-22/lhtype-22: low-redshift low/high-luminosity X-ray obscured optical type-2 AGN;

cantly shallower slope, i.e. photon index  $\Gamma = 1.54 \pm 0.14$ . As shown in Fig. 19, the hhtype-11 has an overall similar stacked spectrum to the lltype-11 as well as the lhtype-11, except for a relatively weak Fe  $K\alpha$  line. Even the X-ray obscured ones, i.e. the hhtype-12 and lhtype-12, does *not* show significant differences. They both have a photon index  $\Gamma \sim 2.04$  and a weak Fe  $K\alpha$  emission line, although a highly ionized emission line is detected in the stacked spectra of hhtype-12.

The estimated  $N_{\text{H}}$  from low S/N X-ray spectra of unobscured type-1 AGN can be higher than  $10^{21} \text{ cm}^{-2}$ , as shown in the simulations by Krumpal et al. (2008). However, only  $\sim 2$  per cent of the sources in the simulations (the sources in those simulations have 40 net photon counts with  $z = 1$ ) showed  $N_{\text{H}}$  higher than  $10^{21.5} \text{ cm}^{-2}$ , which is much smaller than the fraction (i.e.  $> 20$  per cent,  $\sim 10$  per cent if only sources with net photon counts larger than 50 are selected) of the X-ray obscured sources in our sample. We thus conclude that the majority of the type-12 AGN in our sample are truly X-ray obscured. Merloni et al. (2014) suggested that the excess X-ray absorption presented in their high X-ray luminosity high redshift type-12 AGN ( $L_{2-10\text{keV}} > 10^{44} \text{ erg s}^{-1}$ ,  $1.5 < z < 2.5$ ) may be produced by dust-free gas within (or inside) the broad-line region. This suggestion was strengthened in a recent work by Davies et al. (2015). Using a complete volume limited hard X-ray selected AGN sample, the authors argued that at high-luminosity (e.g.  $\log L_{14-195} > 44$ ) the torus consist of two parts, an outer part which is the dusty torus and an inner dust-free part which is responsible for the excess X-ray obscuration. Our work seems to be consistent with this scenario. As shown in Fig. 19, the rest-frame 4 – 25 keV stacked spectra of the hhtype-11 and 12 AGN are almost identical (this seems to also be true for the lhtype-11/12 AGN, though only the spectra below  $\sim 10\text{keV}$  are available). On average, the hhtype-12 AGN do *not* show a stronger reflection component than the hhtype-11, i.e.  $R_{\text{refl}} < 1.7$  for hhtype-12 and  $R_{\text{refl}} = 2.25^{+0.72}_{-0.58}$  for hhtype-11 if we fit the stacked spectra with the  $p_{\text{exrav}}$  model. Both the stacked spectra of the high-luminosity type-12 sub-samples have steep slopes ( $\Gamma \sim 2.04$ ), which is consistent with the slopes found in typical type-1 AGN, showing no



evidence for strong reprocessing of the primary continuum. Moreover, the EWs of the Fe K $\alpha$  line in the high-luminosity type-12 sub-samples are weaker than that found in typical type-2 AGN, e.g.  $\gtrsim 200$  eV (LaMassa et al. 2009). These results may imply that the high-luminosity type-12 AGN have similar torus structure to the typical type-1 AGN. Thus the excess X-ray absorption in the high-luminosity type-12 AGN is more likely to be due to dust-free gas which may probably locate close to or within the BLR, instead of the dusty torus. In addition, a  $\sim 6.67$  keV (i.e.  $E = 6.67 \pm 0.05$  if fitted with a Gaussian model) emission line, which must be the Fe XXV line, is detected in the stacked spectra of htype-12 AGN. This suggest that, when the luminosity is high, the dust-free gas can be ionized by the strong radiation from the central region.

On the contrary, the shallow slope of the power-law continuum as well as the EW of the Fe K $\alpha$  line (see Fig. 20, open magenta circle) are indications that the average X-ray properties of the sources in the low-redshift low-luminosity type-12 (lltype-12) bin are close to the typical type-2 AGN. These results thus suggest that the excess X-ray absorption in the lltype-12 AGN is likely to be due to obscuration by the torus. One possibility is that the low-luminosity sources have on average higher torus covering factor than the high-luminosity ones, i.e. luminosity-dependent dust covering factor as suggested in Section 6.1. This is also in accord with Davies et al. (2015), in which have shown that the opening angle of the dusty torus is smaller at lower luminosity (e.g.  $\log L_{14-195} < 44$ ). The detection of the broad emission line in the optical spectra either suggest that a clumpy torus structure is common in AGN (e.g. Cofey et al. 2014), or could be due to variability obscuration and the non-simultaneous of X-ray/optical observations.

#### 6.4.2 X-ray unobscured type-2 AGN

The stacked spectra for the low/high-luminosity type-2 AGN are shown in the bottom panel of Fig. 18. Both the lltype-22/ltype-22 AGN, which are marked as open/filled red stars in Fig. 20, have X-ray properties of the typical type-2 AGN, i.e. shallow power-law photon indices ( $1.17 \pm 0.16$  for lltype-22 and  $1.62 \pm 0.09$  for ltype-22, the abnormal low photon index of the lltype-22 can be potentially due to the degeneration with column density) and relatively high EWs of Fe K $\alpha$  line ( $284_{-81}^{+105}$  for lltype-22 and  $143_{-49}^{+57}$  for ltype-22). The difference of the EWs of the Fe K $\alpha$  line between the two luminosity bins may imply that the fraction of heavily obscured sources in the low-luminosity type-22 is higher than the high-luminosity ones, i.e. the obscuration fraction decrease with X-ray luminosity (e.g. Merloni et al. 2014, and references therein).

Only upper limits of the column density ( $\sim 5 \times 10^{21}$  cm $^{-2}$ ) can be given for the lltype-21 and ltype-21 AGN. They have very similar X-ray properties, both the EW of Fe K $\alpha$  line as well as the photon index are consistent well within uncertainties.

There are several reasons which may possibly explain the lack of X-ray obscuration in these optical type-2 AGN. The first one is that, due to the low S/N of the X-ray spectra, the  $N_H$  of most sources in the type-21 may actually be underestimated. However, the relatively weak Fe K $\alpha$  line seems to be inconsistent with this explanation. Furthermore, we still have about 40 per cent of X-ray unobscured type-2 AGN even when only sources with higher S/N are selected. It is also possible that these X-ray unobscured type-2 AGN are contaminated by type-1 sources. In Davies et al. (2015), they concluded that the X-ray unabsorbed type-2 AGN are rare and the high fraction of type-21 found in Merloni et al. (2014) is due to a bias in the photometric classification. In our sample, the type-2 sample we used include sources which are classified as type-2 can-

didate (NLAGN2cand) in Menzel et al. (2016). These type-2 candidates mainly consist of low (optical spectroscopic) S/N type-2 AGN, but may also include contaminating star-forming galaxies as well as type-1 AGN. The fraction of type-21 AGN in these sources ( $\sim 55$  per cent) is higher than that in the pure type-2 sample ( $\sim 40$  per cent). In addition, both the pure type-2 and the type-2 candidate sample may include the so-called true type-2 AGN (e.g. Panessa & Bassani 2002; Brightman & Nandra 2008; Shi et al. 2010; Bianchi et al. 2012; Li et al. 2015, see also Shu et al. 2007; Valencia-S. et al. 2012; Ichikawa et al. 2015 and references therein), i.e. AGN without any scattered or hidden BLR signature. The optical type-2 AGN without X-ray obscuration feature can also be explained by including the so-called elusive AGN (eAGN-SFG and eAGN-ALG, see Section 3.2). They can be weak type-1 AGN for which the optical spectra are dominated by the host galaxies. The X-ray column density distribution, with about 75 per cent of these elusive AGN have  $N_H$  less than  $10^{21.5}$  cm $^{-2}$ , seems to support the suggestion that these are more likely to be weak type-1 AGN. Due to relatively small number of type-2 AGN in our sample, we cannot further split the type-21 into different sub-samples (e.g. pure type-2, type-2 candidate and elusive AGN) to investigate which is the main contributor of the X-ray unobscuration. Further studies of large samples with high S/N is necessary to resolve the problem.

## 7 SUMMARY AND CONCLUSION

In this paper, we studied the X-ray properties of a large AGN sample selected in the XXL-N field. In total, 8445 point-like X-ray sources are detected in this field, of which  $\sim 2512$  have reliable redshift measurements as well as optical classifications from a dedicated SDSS-III/BOSS ancillary program. Those sources with redshift measurements are selected as the main AGN sample in this work. The details of the 8445 X-ray detected sources can be found online, while the properties of the sources with redshift measurements are presented in Table 2. By performing the spectral fitting to the BOSS spectroscopy of the type-1 objects in our sample, we estimate the single-epoch virial BH masses from continuum luminosities and broad line widths. To estimate the bolometric luminosity, we calculated the radiation directly produced by the accretion process, i.e. the optical/UV thermal radiation which is computed assuming a standard thin disc and the hard X-ray radiation estimated from the X-ray spectral analysis. The  $M_{BH}$ , bolometric luminosity,  $\lambda_{Edd}$  and other optical properties for the type-1 objects are described in Table 3.

We analysed the X-ray data of our AGN sample by means of X-ray spectral modelling and X-ray spectral stacking. We adopted the BXA software to fit the X-ray spectra of each individual source, in which case the posterior distribution of each parameter can be obtained. In order to investigate how the X-ray properties of AGN changes with the physical parameters, e.g. the X-ray luminosity, redshift,  $M_{BH}$ ,  $\lambda_{Edd}$  and column density, a X-ray spectral stacking method is applied to different sub-samples, which are selected on the basis of the AGN physical parameters.

The main results of our study are summarized below.

(i) We confirm the well-known X-ray Baldwin effect in our luminosity-redshift sub-samples, i.e. a decrease of the equivalent width of the narrow Fe K $\alpha$  line with increasing X-ray luminosity. Furthermore, we find that the low luminosity, low-redshift sub-sample has a systematically higher reflection fraction than the high-redshift/low-redshift, high-luminosity one. These results are in good

agreement with the view that the X-ray Baldwin effect is due to the decrease in the covering factor of the torus with X-ray luminosity.

(ii) By comparing the photon index measured from the three  $\lambda_{\text{Edd}}$  sub-samples, we find evidence for a decreasing or constant photon index at high  $\lambda_{\text{Edd}}$ , which is contrary to previous works. We suggest that the structure of the accretion disc may change as the Eddington ratio approaches unity.

(iii) Following Merloni et al. (2014), We investigated the properties of the type-11/12 AGN sample by the X-ray spectral stacking method. We did not find any evidence for a higher reflection fraction in the high-luminosity type-12 sample comparing with high-luminosity type-11 sample. We thus suggested that the excess X-ray absorption shown in those optical broad line AGN can be due to small scale dust-free gas within (or close) to the BLR. However, the stacked X-ray spectrum of the low-luminosity type-12 sample has a shallower slope than the type-11 counterpart. This is an indication that the X-ray obscuration in those objects may be due to a clumpy torus with large covering factor.

(iv) The situation of the type-21/22 AGN is more complicated and less clear, due to a relatively small number of type-2 AGN in our sample. One possible explanation for the lack of X-ray obscuration in the type-21 AGN is the contamination from star-forming galaxies, type-1 AGN, true type-2 AGN or the elusive type-2 AGN. Future X-ray studies with large spectroscopic type-2 AGN samples, such as those selected with eROSITA (Merloni et al. 2012), can help to resolve this problem.

## 8 ACKNOWLEDGEMENTS

ZL thanks Murray Brightman, Tom Dwelly, Kazushi Iwasawa, Yuan Liu, Youjun Lu, Xinwen Shu and Weimin Yuan for useful discussions. Thanks are given to Damien Coffey for a careful read of the manuscript. ZL is grateful for the support by the MPG–CAS Joint Doctoral Promotion Programme and the hospitality of MPE, where the research was carried out. This work benefited from the thales project 383549 that is jointly funded by the European Union and the Greek Government in the framework of the programme ‘Education and lifelong learning’. Funding for SDSS-III has been provided by the Alfred P. Sloan Foundation, the Participating Institutions, the National Science Foundation, and the U.S. Department of Energy Office of Science. The SDSS-III web site is <http://www.sdss3.org/>.

SDSS-III is managed by the Astrophysical Research Consortium for the Participating Institutions of the SDSS-III Collaboration including the University of Arizona, the Brazilian Participation Group, Brookhaven National Laboratory, Carnegie Mellon University, University of Florida, the French Participation Group, the German Participation Group, Harvard University, the Instituto de Astrofísica de Canarias, the Michigan State/Notre Dame/JINA Participation Group, Johns Hopkins University, Lawrence Berkeley National Laboratory, Max Planck Institute for Astrophysics, Max Planck Institute for Extraterrestrial Physics, New Mexico State University, New York University, Ohio State University, Pennsylvania State University, University of Portsmouth, Princeton University, the Spanish Participation Group, University of Tokyo, University of Utah, Vanderbilt University, University of Virginia, University of Washington, and Yale University.

## REFERENCES

- Abramowicz M. A., Czerny B., Lasota J. P., Szuszkiewicz E., 1988, *ApJ*, 332, 646
- Ai Y. L., Yuan W., Zhou H. Y., Wang T. G., Zhang S. H., 2011, *ApJ*, 727, 31
- Aihara H., et al., 2011, *ApJS*, 193, 29
- Akylas A., Georgantopoulos I., Georgakakis A., Kitsionas S., Hatziminaoglou E., 2006, *A&A*, 459, 693
- Antonucci R., 1993, *ARA&A*, 31, 473
- Antonucci R. R. J., Miller J. S., 1985, *ApJ*, 297, 621
- Arévalo P., et al., 2014, *ApJ*, 791, 81
- Arnaud K. A., 1996, *ASPC*, 101, 17
- Bauer F. E., et al., 2015, *ApJ*, 812, 116
- Bianchi S., Guainazzi M., Matt G., Fonseca Bonilla N., 2007, *A&A*, 467, L19
- Bianchi S., et al., 2012, *MNRAS*, 426, 3225
- Bolton A. S., et al., 2012, *AJ*, 144, 144
- Bongiorno A., et al., 2010, *A&A*, 510, A56
- Boroson T. A., Green R. F., 1992, *ApJS*, 80, 109
- Brandt W. N., Alexander D. M., 2015, *A&AR*, 23, 1
- Brenneman L. W., Reynolds C. S., 2006, *ApJ*, 652, 1028
- Brightman M., et al., 2015, *ApJ*, 805, 41
- Brightman M., et al., 2013, *MNRAS*, 433, 2485
- Brightman M., Nandra K., 2008, *MNRAS*, 390, 1241
- Brightman M., Nandra K., 2011, *MNRAS*, 413, 1206
- Brusa M., et al., 2010, *ApJ*, 716, 348
- Buchner J., et al., 2014, *A&A*, 564, A125
- Buchner J., et al., 2015, *ApJ*, 802, 89
- Clerc N., et al., 2014, *MNRAS*, 444, 2723
- Chaudhary P., Brusa M., Hasinger G., Merloni A., Comastri A., 2010, *A&A*, 518, A58
- Coffey D., et al., 2014, *MNRAS*, 443, 1788
- Constantin A., Green P., Aldcroft T., Kim D.-W., Haggard D., Barkhouse W., Anderson S. F., 2009, *ApJ*, 705, 1336
- Corral A., et al., 2008, *A&A*, 492, 71
- Dauser T., Wilms J., Reynolds C. S., Brenneman L. W., 2010, *MNRAS*, 409, 1534
- Davies R., et al., 2015, *ApJ*, 806, 127
- Davis S. W., Laor A., 2011, *ApJ*, 728, 98
- de La Calle Pérez I., et al., 2010, *A&A*, 524, A50
- Elvis M., et al., 1994, *ApJS*, 95, 1
- Fabian A. C., Rees M. J., Stella L., White N. E., 1989, *MNRAS*, 238, 729
- Fabian A. C., et al., 2009, *Nature*, 459, 540
- Falocco S., Carrera F. J., Barcons X., Miniutti G., Corral A., 2014, *A&A*, 568, A15
- Falocco S., et al., 2013, *A&A*, 555, A79
- Falocco S., Carrera F. J., Corral A., Laird E., Nandra K., Barcons X., Page M. J., Digby-North J., 2012, *A&A*, 538, A83
- Fanali R., Caccianiga A., Severgnini P., Della Ceca R., Marchese E., Carrera F. J., Corral A., Mateos S., 2013, *MNRAS*, 433, 648
- Gabriel C., et al., 2004, *ASPC*, 314, 759
- Georgakakis A., Nandra K., 2011, *MNRAS*, 414, 992
- Georgakakis A., Nandra K., Laird E. S., Aird J., Trichas M., 2008, *MNRAS*, 388, 1205
- George I. M., Fabian A. C., Nandra K., 1990, *MNRAS*, 242, 28P
- Gu M., Cao X., 2009, *MNRAS*, 399, 349
- Haardt F., Maraschi L., 1991, *ApJ*, 380, L51
- Haardt F., Maraschi L., 1993, *ApJ*, 413, 507
- Harrison F. A., et al., 2013, *ApJ*, 770, 103
- Hasinger G., 2008, *A&A*, 490, 905
- Ichikawa K. et al., 2015, *ApJ*, 803, 57
- Iwasawa K., et al., 2012, *A&A*, 546, AA84
- Iwasawa K., Taniguchi Y., 1993, *ApJ*, 413, L15
- Jansen F., et al., 2001, *A&A*, 365, L1
- Jiang P., Wang J. X., Wang T. G., 2006, *ApJ*, 644, 725
- Jiménez-Bailón E., Piconcelli E., Guainazzi M., Schartel N., Rodríguez-Pascual P. M., Santos-Lleó M., 2005, *A&A*, 435, 449

- Jin C., Ward M., Done C., 2012, *MNRAS*, 425, 907
- Kalberla P. M. W., Burton W. B., Hartmann D., Arnal E. M., Bajaja E., Morras R., Pöppel W. G. L., 2005, *A&A*, 440, 775
- Kamizasa N., Terashima Y., Awaki H., 2012, *ApJ*, 751, 39
- Kormendy J., Richstone D., 1995, *ARA&A*, 33, 581
- Krolik J. H., 1999, *agnc.book*,
- Krumpe M., et al., 2008, *A&A*, 483, 415
- Krumpe M., Lamer G., Markowitz A., Corral A., 2010, *ApJ*, 725, 2444
- Kuntz K. D., Snowden S. L., 2010, *ApJS*, 188, 46
- Laird E. S., et al., 2009, *ApJS*, 180, 102
- LaMassa S. M., Heckman T. M., Ptak A., Hornschemeier A., Martins L., Sonnentrucker P., Tremonti C., 2009, *ApJ*, 705, 568
- Liu Y., Li X., 2015, *MNRAS*, 448, L53
- Liu Y., Li X., 2014, *ApJ*, 787, 52
- Li Y., Yuan W., Zhou H. Y., Komossa S., Ai Y. L., Liu W. J., Boisvert J. H., 2015, *AJ*, 149, 75
- Liu Z., Yuan W., Lu Y., Zhou X., 2015, *MNRAS*, 447, 517
- Lu Y., Yu Q., 1999, *ApJ*, 526, L5
- Lusso E., et al., 2012, *MNRAS*, 425, 623
- Magdziarz P., Zdziarski A. A., 1995, *MNRAS*, 273, 837
- Maggi P., et al., 2014, *A&A*, 561, AA76
- Marconi A., Risaliti G., Gilli R., Hunt L. K., Maiolino R., Salvati M., 2004, *MNRAS*, 351, 169
- Menzel M.-L., et al., 2016, *MNRAS*, 457, 110
- Merloni A., et al., 2014, *MNRAS*, 437, 3550
- Merloni A., et al., 2012, *arXiv*, arXiv:1209.3114
- Merloni A., Heinz S., 2008, *MNRAS*, 388, 1011
- Miller L., Turner T., Reeves J., 2008, *A&A*, 452, 437
- Murphy K. D., Yaqoob T., 2009, *MNRAS*, 397, 1549
- Nandra K., George I. M., Mushotzky R. F., Turner T. J., Yaqoob T., 1997, *ApJ*, 488, L91
- Nandra K., Pounds K. A., 1994, *MNRAS*, 268, 405
- Nandra K., O'Neill P. M., George I. M., Reeves J. N., 2007, *MNRAS*, 382, 194
- Nayakshin S., 2000, *ApJ*, 534, 718
- Page K. L., O'Brien P. T., Reeves J. N., Turner M. J. L., 2004, *MNRAS*, 347, 316
- Panessa F., Bassani L., 2002, *A&A*, 394, 435
- Patrick A. R., Reeves J. N., Porquet D., Markowitz A. G., Braito V., Lobban A. P., 2012, *MNRAS*, 426, 2522
- Pierre M., et al., 2007, *MNRAS*, 382, 279
- Pierre M., et al., 2015, *arXiv*, arXiv:1512.04317
- Pounds K. A., Done C., Osborne J. P., 1995, *MNRAS*, 277, L5
- Pounds K. A., Nandra K., Stewart G. C., George I. M., Fabian A. C., 1990, *Nature*, 344, 132
- Reeves J. N., Turner M. J. L., 2000, *MNRAS*, 316, 234
- Ricci C., Paltani S., Awaki H., Petrucci P.-O., Ueda Y., Brightman M., 2013, *A&A*, 553, AA29
- Ricci C., Paltani S., Ueda Y., Awaki H., 2013, *MNRAS*, 435, 1840
- Ricci C., Ueda Y., Paltani S., Ichikawa K., Gandhi P., Awaki H., 2014, *MNRAS*, 441, 3622
- Richards G. T., et al., 2006, *ApJS*, 166, 470
- Risaliti G., Lusso E., 2015, *ApJ*, 815, 33
- Risaliti G., Maiolino R., Salvati M., 1999, *ApJ*, 522, 157
- Risaliti G., Young M., Elvis M., 2009, *ApJ*, 700, L6
- Salviander S., Shields G. A., Gebhardt K., Bonning E. W., 2007, *ApJ*, 662, 131
- Shakura N. I., Sunyaev R. A., 1973, *A&A*, 24, 337
- Shankar F., 2009, *NewAR*, 53, 57
- Shemmer O., Brandt W. N., Netzer H., Maiolino R., Kaspi S., 2008, *ApJ*, 682, 81
- Shemmer O., Brandt W. N., Netzer H., Maiolino R., Kaspi S., 2006, *ApJ*, 646, L29
- Shen Y., 2013, *BASI*, 41, 61
- Shen Y., et al., 2011, *ApJS*, 194, 45
- Shen Y., Greene J. E., Strauss M. A., Richards G. T., Schneider D. P., 2008, *ApJ*, 680, 169
- Shen Y., Ho L. C., 2014, *Nature*, 513, 210
- Shen Y., Liu X., 2012, *ApJ*, 753, 125
- Shi Y., Rieke G. H., Smith P., Rigby J., Hines D., Donley J., Schmidt G., Diamond-Stanic A. M., 2010, *ApJ*, 714, 115
- Shu X. W., Yaqoob T., Wang J. X., 2011, *ApJ*, 738, 147
- Shu X. W., Yaqoob T., Wang J. X., 2010, *ApJS*, 187, 581
- Shu X. W., Wang J. X., Jiang P., Fan L. L., Wang T. G., 2007, *ApJ*, 657, 167
- Shu X. W., Wang J. X., Yaqoob T., Jiang P., Zhou Y. Y., 2012, *ApJ*, 744, L21
- Stoughton C., et al., 2002, *AJ*, 123, 485
- Streblyanska A., Hasinger G., Finoguenov A., Barcons X., Mateos S., Fabian A. C., 2005, *A&A*, 432, 395
- Strüder L., et al., 2001, *A&A*, 365, L18
- Sturm, R. K. N. 2012, PhD thesis, Fakultät für Physik, Technische Universität München, Germany
- Sutherland W., Saunders W., 1992, *MNRAS*, 259, 413
- Tanaka Y., et al., 1995, *Nature*, 375, 659
- Tatum M. M., Turner T. J., Sim S. A., Miller L., Reeves J. N., Patrick A. R., Long K. S., 2012, *ApJ*, 752, 94
- Trouille L., Barger A. J., Cowie L. L., Yang Y., Mushotzky R. F., 2009, *ApJ*, 703, 2160
- Tsuzuki Y., Kawara K., Yoshii Y., Oyabu S., Tanabé T., Matsuoka Y., 2006, *ApJ*, 650, 57
- Turner M. J. L., et al., 2001, *A&A*, 365, L27
- Turner T. J., George I. M., Nandra K., Mushotzky R. F., 1997, *ApJ*, 488, 164
- Turner T. J., Miller L., 2009, *A&AR*, 17, 47
- Turner T. J., Pounds K. A., 1989, *MNRAS*, 240, 833
- Ueda Y., Akiyama M., Ohta K., Miyaji T., 2003, *ApJ*, 598, 886
- Ueda Y., et al., 2008, *ApJS*, 179, 124
- Urry C. M., Padovani P., 1995, *PASP*, 107, 803
- Valencia-S., M., Zuther, J., Eckart, A., et al. 2012, *A&A*, 544, A129
- Vasudevan R. V., Fabian A. C., 2007, *MNRAS*, 381, 1235
- Vasudevan R. V., Fabian A. C., 2009, *MNRAS*, 392, 1124
- Vasudevan R. V., Mushotzky R. F., Winter L. M., Fabian A. C., 2009, *MNRAS*, 399, 1553
- Vestergaard M., Peterson B. M., 2006, *ApJ*, 641, 689
- Vestergaard M., Wilkes B. J., 2001, *ApJS*, 134, 1
- Volonteri M., Sikora M., Lasota J.-P., Merloni A., 2013, *ApJ*, 775, 94
- Wang J.-M., Watarai K.-Y., Mineshige S., 2004, *ApJ*, 607, L107
- Watson M. G., et al., 2009, *A&A*, 493, 339
- Weisskopf M. C., Tananbaum H. D., Van speybroeck L. P., O'Dell S. L., 2000, *SPIE*, 4012, 2
- Wu Q., Gu M., 2008, *ApJ*, 682, 212
- Younes G., Porquet D., Sabra B., Reeves J. N., 2011, *A&A*, 530, A149
- Zhou X.-L., Wang J.-M., 2005, *ApJ*, 618, L83
- Zhou X.-L., Zhao Y.-H., 2010, *ApJ*, 720, L206

## APPENDIX A: XMM OBSERVATION LOG

The individual XMM observations used in this paper is listed in Table A. In addition to the XXL-N/XMM-LSSS 10ks data, deeper XMM observations within the XXL-N footprint are also included.

## APPENDIX B: TABLE COLUMNS

The information of the full catalogue (see Section 3.1) is list here. The full list can be found online.

### B1 source detection parameters

uxid (30a): unique x-ray source identification string. the unique name of the each source is a string which is composed from the project name, followed by the number of the pointing on which the

**Table A1.** XMM-XXL log of observations

XMM obsid	RA	DEC	EPIC-PN		EPIC-MOS1		EPIC-MOS2	
	J2000		filter	exposure (s)	filter	exposure (s)	filter	exposure (s)
0037980101	02:22:45.61	-03:50:57.3	Thin1	10178	Thin1	14560	Thin1	14552
0037980201	02:24:05.66	-03:50:58.4	Thin1	8999	Thin1	13375	Thin1	13235
0037980301	02:25:25.73	-03:50:57.8	Thin1	9100	Thin1	13476	Thin1	13436
0037980401	02:26:45.47	-03:50:59.1	Thin1	3680	Thin1	6020	Thin1	5340
0037980501	02:28:05.38	-03:51:00.7	Thin1	12268	Thin1	16066	Thin1	16051

Log of the XMM observations used to construct the X-ray source catalogue in the equatorial XMM-XXL field. Listed are (1) XMM observation identification number. A “U” at the end of the observation ID marks “unscheduled” XMM observations. Data taken in the XMM mosaic mode are marked by a trailing incremental number separated by the observations identification number by an underscore. (2) Right Ascension of the XMM observation in J2000, (3) Declination of the XMM observation in J2000, (4) EPIC PN filter used during the observations, (5) EPIC PN exposure time in seconds, (6) EPIC MOS1 filter used during the observations, (7) EPIC MOS2 exposure time in seconds, (8) EPIC MOS2 filter used during the observations, (9) EPIC MOS2 exposure time in seconds. The full list can be found online.

source is detected or zero in the case of projects with a single xmm observation and ending with a sequential number.

box\_id\_src (j): identification number of a source on individual pointings or observations in the case of projects with a single xmm observation.

ra (d): right ascension in degrees of the x-ray source before correcting for systematic offsets.

dec (d): declination in degrees of the x-ray source before correcting for systematic offsets.

radec\_err (e): positional uncertainty in arcsec of the source position. this parameter is estimated by the EWAVELET task of sas.

This paper has been typeset from a  $\text{\TeX}/\text{\LaTeX}$  file prepared by the author.

## B2 Source parameters related to flux estimation

CNT\_TOTAL\_FULLL\_80 (J): full band counts at the source position from all EPIC cameras estimated within the 80 per cent EEf ellipse.

BKG\_TOTAL\_FULLL\_80 (E): expected number of full band background counts at the source position from all EPIC cameras within the 80 per cent EEf ellipse.

EXP\_TOTAL\_FULLL\_80 (E): full band exposure time in seconds at the source position from all EPIC cameras. This parameter is the average exposure time within the 80 per cent EEf ellipse.

CNT\_PN\_FULLL\_80 (J): full band counts at the source position on the PN camera within the 80 per cent EEf ellipse.

## B3 X-ray optical identification parameters

SDSS\_ID (20A): SDSS source identification number.

RA\_OPT (E): SDSS optical counterpart Right Ascension (J2000).

DEC\_OPT (E): SDSS optical counterpart Declination (J2000).

## B4 SDSS photometry parameters

petro\_u (E): SDSS *u*-band petrosian magnitude of the optical counterpart.

petro\_g (E): SDSS *g*-band petrosian magnitude of the optical counterpart.

petro\_r (E): SDSS *r*-band petrosian magnitude of the optical counterpart.

petro\_i (E): SDSS *i*-band petrosian magnitude of the optical counterpart.

petro\_z (E): SDSS *z*-band petrosian magnitude of the optical counterpart.